Multi-Fidelity Design of an Aeroelastically Tailored Composite Wing for Dynamic Wind-Tunnel Testing

Mitrotta, F.M.A.; Rajpal, Darwin; Sodja, Jurij; De Breuker, Roeland

DOI
10.2514/6.2020-1636

Publication date
2020

Document Version
Final published version

Published in
AIAA Scitech 2020 Forum

Citation (APA)
Mitrotta, F. M. A., Rajpal, D., Sodja, J., & De Breuker, R. (2020). Multi-Fidelity Design of an Aeroelastically Tailored Composite Wing for Dynamic Wind-Tunnel Testing. In *AIAA Scitech 2020 Forum: 6-10 January 2020, Orlando, FL* Article AIAA 2020-1636 (AIAA Scitech 2020 Forum; Vol. 1 PartF). American Institute of Aeronautics and Astronautics Inc. (AIAA). https://doi.org/10.2514/6.2020-1636

AIAA SciTech Forum
6-10 January 2020, Orlando, FL
AIAA Scitech 2020 Forum

10.2514/6.2020-1636

Multi-Fidelity Design of an Aeroelastically Tailored Composite Wing for Dynamic Wind-Tunnel Testing

Francesco M. A. Mitrotta[*], Darwin Rajpal[†], Jurij Sodja[‡] and Roeland De Breuker[§]
Delft University of Technology, The Netherlands

Aeroelastic tailoring offers an effective way to exploit the anisotropic properties of the composite materials used in lightweight aerospace structures. This paper presents a design methodology for experimental wings that employ a typical wingbox structure. The proposed methodology combines three different analysis tools: Proteus, a low-fidelity aeroelastic framework with tailoring capabilities, OptiBLESS, an open-source toolbox for optimization of blended stacking sequences and MSC Nastran, a commercial software commonly used in industry for aeroelastic analyses. An experimental wing is designed using the proposed framework. The developed design is manufactured using carbon fibre pre-preg and hand layup technique. Finally, the manufactured wing is tested in the wind-tunnel at speeds up to 25 m/s. Both static and dynamic tests are performed, where for the latter a gust generator is used. The experimental results provide a source of comparison for the numerical models used in the proposed design methodology.

I. Nomenclature

$\boldsymbol{A}$ = membrane stiffness matrix
$\hat{\boldsymbol{A}}$ = thickness-normalized membrane stiffness matrix
b = flange width
$\boldsymbol{D}$ = bending stiffness matrix
$\hat{\boldsymbol{D}}$ = thickness-normalized bending stiffness matrix
E_{11} = ply longitudinal Young's modulus
E_{22} = ply transversal Young's modulus
f = objective function
f_g = gust frequency
G_{12} = ply shear modulus
h_b = buckling index in terms of ratio between applied and failure load
h_s = strain index in terms of ratio between applied and failure load
k_b = buckling constraint correction coefficient
k_s = strain constraint correction coefficient
S = ply shear strength
t = laminate thickness
$\boldsymbol{t}$ = vector of laminates' thickness
t_{ply} = ply thickness
$\boldsymbol{V}$ = vector of laminates' lamination parameters
V_g = gust velocity
$\boldsymbol{V_p}$ = vector of laminates' lamination parameters resulting from optimization
$\widetilde{\boldsymbol{V_p}}$ = vector of laminates' lamination parameters resulting from stacking sequence retrieval
V_∞ = free-stream velocity

---

[*] MSc Student, Faculty of Aerospace Engineering, Aerodynamics, Kluyverweg 2 2629 HS Delft, F.M.A.Mitrotta-1@student.tudelft.nl.

[†] PhD Candidate, Faculty of Aerospace Engineering, Aerospace Structures and Computational Mechanics, Kluyverweg 1 2629 HS Delft, D.Rajpal@tudelft.nl, AIAA Student Member.

[‡] Senior scientist, Faculty of Aerospace Engineering, Aerospace Structures and Computational Mechanics, Kluyverweg 1 2629 HS Delft, J.Sodja@tudelft.nl, AIAA Member.

[§] Associate Professor, Faculty of Aerospace Engineering, Aerospace Structures and Computational Mechanics, Kluyverweg 1 2629 HS Delft, R.deBreuker@tudelft.nl, AIAA Senior Member.

$\boldsymbol{x}$ = vector of design variables
X_c = ply longitudinal compressive strength
X_t = ply longitudinal tensile strength
Y_c = ply transversal compressive strength
Y_t = ply transversal tensile strength
γ_{max} = maximum shear strain
Δz_{tip} = tip displacement
$\Delta\alpha_g$ = gust incremental angle of attack
$\Delta\alpha_{gv}$ = gust vanes' actuation angle
ϵ_{max} = major principal strain
ϵ_{min} = minor principal strain
ρ = density
σ_c^u = laminate's ultimate compressive strength
σ_{crip} = crippling stress
ν_{12} = ply Poisson's ratio

II. Introduction

The reduction of CO2, NOx and noise emissions is one of the challenges of both current and future transport aircraft industry. This is testified by related goals set by international institutions, such as European Union with the *Flightpath 2050* document [1], and by research organizations, such as NASA with its *Fixed Wing* project [2]. A common design objective that pursues reduction of fuel burn and consequently of emissions is the realization of lightweight structures, which have been extensively applied in aircraft design thanks to the use of composite materials. These are characterized not only by a high specific strength and stiffness, but also by an anisotropic behaviour that allows designers to tailor the structure according to specific needs. This is also known as aeroelastic tailoring, which has been subject of extensive research over the last decades.

A summary of research into aeroelastic tailoring methodologies for transport aircraft wings was given by Jutte and Stanford [3]. As far as experimental work is concerned, early studies focused on the investigation of plate structures, where the bend-twist coupling of the overall structure originates directly from the bend-twist coupling of the laminate [4–8]. However, the structure of a representative transport aircraft wing is given by the closed-cell cross-sectional configuration called wingbox, where the bend-twist coupling mechanism is different from the one present in plates. In fact, for a wingbox structure the bend-twist coupling at the wing level is obtained thanks to the extension-shear coupling of the individual laminates of the cross-section.

With the aim of studying structures involving the extension-shear coupling mechanism, more recent experimental investigations focused on testing wings employing tailored composite skins. For example, a complete cycle of optimization, manufacturing and testing of a rectangular unswept aeroelastically tailored wing was presented by Meddaikar et al. [9]. The wing was designed by means of a two-step optimization process, where first a gradient-based optimization in lamination parameter domain was carried out and afterwards a genetic algorithm was used for stacking sequence optimization. Both steps employed a maximum tip deflection objective, with variable thickness and stiffness along the span. The optimized wing was manufactured and static wind-tunnel tests were performed. A follow-up of this work was presented in [10], where the same aeroelastic tailoring framework was applied to the design of three different forward swept wings. Two of these wings were again optimized for maximum tip deflection, however this time an additional constraint was imposed to prevent wash-in in order to counter the inherent divergence issues pertinent to forward swept wings. Results from static wind-tunnel tests were provided in terms of wing deformation and lift. Despite the valuable experimental validation data provided for wings employing tailored composite skins, in both mentioned studies the tested wings were filled with foam and they were thus missing an internal structure representative of a transport aircraft wing. In fact, for both studies the authors mentioned the need for numerical model update, either due to the need of better modelling of the clamp or due to idealizations in the finite element model.

Another example of optimization, manufacturing and wind-tunnel testing of an aeroelastically tailored wing is given by studies conducted in the last years at Delft University of Technology (TUD). A dynamic aeroelastic framework with tailoring capabilities for conceptual design of composite wing structures was introduced by Werter and De Breuker [11]. This framework is based on gradient-based optimization in the lamination parameter domain employing a geometrically nonlinear beam model with variable thickness and stiffness. Its application to the design of a rectangular unswept composite wing with tailored skins was presented in [12]. The designed wing employed constant thickness and stiffness along the span, so that a manufacturable stacking sequence could be found by a simple sweep over ply angles. Also in this case the internal structure of the wing was constituted by foam. First, a static structural test was carried out to characterize the wing and update the numerical beam model. Next, wind-tunnel tests were performed providing experimental validation data for the aeroelastic framework. During another experimental campaign, the same wing was tested under dynamic conditions in a wind-tunnel environment, as discussed by Sodja et al. [13]. Various dynamic cases were tested by harmonically pitching the wing at different pitching frequencies, mean pitch angles and free-stream velocities. In this way the unsteady aerodynamic effects from quasi-steady to highly unsteady conditions were covered.

Although the wings designed and manufactured in the mentioned works [9, 10, 12] employ tailored composite skins, they all feature foam as internal structure in place of spars and ribs. Therefore, on one hand those wings represent a step closer to industrial practice with respect to plate structures, but on the other hand they are not entirely representative of a realistic wing as they miss the typical wingbox structure. Considering the field of general aeroelastic testing, another application of composite skins and wing foam core is given by the work of Timmermans et al. [14], where a highly elastic fiberglass wing-body pylon nacelle model was tested. In this case a D-spar was also included in the wing. A different concept of aeroelastic wind-tunnel model was given by the use of a single beam carrying the loads and some sort of aerodynamic fairing providing the airfoil shape [15–19]. Only Freydin et al. [20] tested an elastic wing model employing a configuration very close to a wingbox structure. This was made out of two rectangular cross-sectioned spars, plates connecting the two spars and a laminate film wrapped around very thin ribs. All the parts except the skin were printed in rapid prototyping. This discussion indicates that, beyond aeroelastic tailoring, also when dealing with other fields of aeroelastic testing the use of wingbox structures is barely found in literature. Consequently, the design, manufacturing and testing of an aeroelastically tailored composite wing with a typical wingbox structure would at the same time advance the state-of-the-art of aeroelastically tailored experimental wings and fill a gap for general aeroelastic wind-tunnel testing.

In this paper a design methodology is proposed for the design of an aeroelastically tailored wing employing a typical wingbox structure comprising skins, spars and ribs. When employing low-fidelity preliminary design tools such as the aeroelastic framework used at TUD, two main challenges arise. The first challenge concerns the reliable assessment of the buckling behaviour of skin panels, while the second consists in a proper modelling of the internal structure including spar web and flanges so that crippling behaviour can be assessed. In order to successfully deal with these challenges, the low-fidelity aeroelastic framework available at TUD is complemented with a medium-fidelity modelling strategy. This is also used to assess the level of conservativeness of the low-fidelity optimization framework and to alleviate its level of conservativeness. Furthermore, in order to allow for the use of variable thickness and stiffness along the wing span, an open-source stacking sequence retrieval toolbox is used to transform the optimization results from lamination parameters into a set of manufacturable blended laminates. The discussed methodology is applied to the design of a rectangular unswept wing, which is manufactured and tested in a wind-tunnel environment for both static and dynamic conditions, where the latter is achieved by gust excitation.

The paper is organized as follows. First, the methodology is discussed in detail with focus on the tools used, the workflow and the interfaces between the tools. Next, the optimization setup and the design problem are described. In the following section the numerical results of the final design are shown, focusing on the effects of the stacking sequence retrieval process and on the comparison between the low-fidelity and the medium-fidelity models. Finally, the results of the wind-tunnel campaign are reported and compared with the numerical models, followed by the conclusions of the paper.

III. Design Framework

A. Framework Tools

The methodology proposed in this paper makes use of three main tools: a low-fidelity aeroelastic tailoring framework called Proteus, an open-source stacking-sequence-retrieval algorithm and a medium-fidelity aeroelastic model implemented in a commercial software.

Proteus is developed in-house at Delft University of Technology. Its main characteristic is the representation of the three-dimensional structure of a wing by means of a 1D Timoshenko beam model obtained through a cross-sectional modeller. The wing geometry is defined by the planform and the airfoil sections. At the same time, the structure is defined by means of several distinct laminates along the span for each of the main structural components: bottom skin, top skin and spars. A cross-sectional analysis is then employed to generate the 1D beam model from the cross-sectional geometry and the laminates' properties. These laminates are described in terms of lamination parameters and laminate thickness, leading to a set of continuous design variables. In this way, a gradient-based optimization algorithm can be employed within the framework. The structural model is then coupled to a vortex lattice aerodynamic model. A detailed explanation of PROTEUS and of the mentioned cross-sectional analysis is given in [11] and [21], respectively.

The second tool employed in the present design framework is called OPTIBLESS, an open-source toolbox for optimization of blended stacking sequence. OPTIBLESS employs a patch-based optimization integrated with a blending strategy to obtain a blended stacking sequence from several sets of lamination parameters representing different neighbouring laminates. The stacking sequence is considered blended when the plies of the thinnest laminate patch span the entire structural component considered. Within the present design framework, OPTIBLESS is used to obtain blended stacking sequences and thus manufacturable laminates for bottom skin, top skin and spars from the optimal lamination parameters computed by PROTEUS. A detailed explanation of the capabilities and the methodologies employed in OPTIBLESS is given by Macquart [22].

Finally, the medium-fidelity aeroelastic model is implemented in MSC NASTRAN, thus allowing for analyses of higher fidelity with respect to the ones possible with PROTEUS. A MATLAB routine is developed to translate the 1D beam model in PROTEUS to a 2D shell model in MSC NASTRAN, making use of the wing geometry and of the laminates' properties. A Doublet Lattice Method (DLM) for aerodynamic load calculation is coupled to the structural model using interpolation methods, denoted as *splining* and already available in MSC NASTRAN. The reason for using a medium-fidelity aeroelastic model is threefold. The first requirement is to have a numerical model including the spar flanges, which are not modelled in PROTEUS. This is necessary in order to verify that the flange is sufficiently strong to resist crippling (further details are given in Section III.B). Another reason for a medium-fidelity aeroelastic model is the need for correction of PROTEUS optimization constraints. In fact, structural constraints such as the ones of buckling and strain are overly conservative in PROTEUS due to modeling assumptions. In this context, the NASTRAN model is used to assess the level of conservativeness of PROTEUS analysis and apply a correction. Finally, the last reason for using a medium-fidelity aeroelastic model lies in the fact that the stacking sequence retrieval process has the inevitable effect of modifying the optimal design and thus both the thickness and stiffness of the laminates. It is then necessary to reliably assess the absence of structural instabilities such as buckling over the entire wing structure.

B. Flow Diagram

A representation of the flow diagram followed within the proposed design methodology is given in Fig. 1. First, the inputs of the optimization are defined. These include the wing geometry, the load cases and the partitioning of the wing in several laminates in order to establish the design variables. Each laminate is described by 8 lamination parameters and its thickness, resulting in 9 design variables per laminate*. An initial value of such variables has to be specified and the optimization problem must be defined in terms of optimization objective and constraints. Furthermore, an initial width is chosen for the flange, which will be used later for the generation of the NASTRAN model of the wing.

The general optimization problem of PROTEUS is formulated as it follows:

$$\begin{aligned} \text{minimize} \quad & f(\boldsymbol{x}) \\ \text{with respect to} \quad & \boldsymbol{V}, \boldsymbol{t} \\ \text{subject to} \quad & h_s(\boldsymbol{V}, \boldsymbol{t}, \text{load cases}) < \frac{1}{1.5} \\ & h_b(\boldsymbol{V}, \boldsymbol{t}, \text{load cases}) < \frac{1}{1.5} \\ & \text{other constraints.} \end{aligned} \tag{1}$$

f is the function to be minimized, which can be the weight of the wing but it is not necessarily limited to that. $\boldsymbol{x}$ is the vector of design variables that the objective function depends on. This vector may include both the thicknesses and lamination parameters of all laminates, respectively $\boldsymbol{t}$ and $\boldsymbol{V}$, depending on the chosen objective function. The two main constraints are formulated in terms of strain index h_s and buckling index h_b. These two indices represent the ratio between the applied load and the failure load, meaning that if $h_s < 1$ there is no strength failure and if $h_b < 1$ there is no buckling failure. A safety factor of 1.5 is applied to both indexes, constraining them to be lower than $1/1.5$. Finally, other constraints that may be imposed within the optimization problem include aeroelastic stability, maximum local angle of attack [11] and blending constraint in the lamination parameters domain [23].

The optimization carried out in PROTEUS results in a set of optimized laminates defined in the lamination parameter domain. At this point, a MATLAB routine groups together the optimal design variables belonging to the same structural

---

[*] Only in-plane and bending lamination parameters are used. Coupling lamination parameters are set to 0 in order to enforce symmetric laminates.

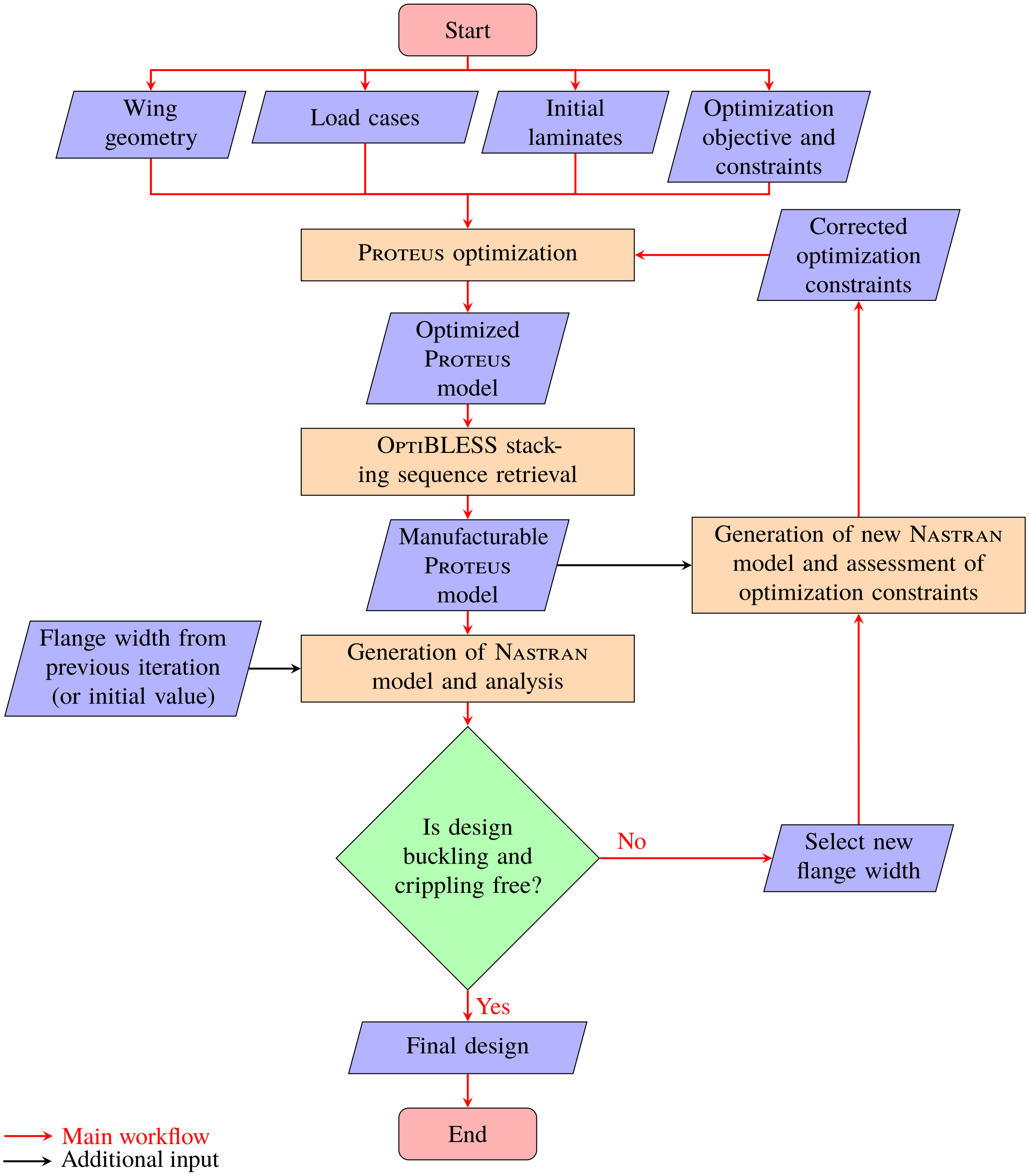

Fig. 1 Flow diagram of the design framework.

part (bottom skin, top skin or spar) in order to feed OptiBLESS and retrieve a set of blended stacking sequences. For each structural part the following optimization problem is solved [22]:

$$\begin{aligned} \text{minimize} \quad & f\left(\boldsymbol{V_p}\right) = \frac{1}{N_{lam}} \sum_{p=1}^{N_{lam}} RMSE_p\left(\boldsymbol{V_p}\right) \\ & RMSE_p = \sqrt{\frac{1}{8}\sum_{i=1}^{8}\left(\widetilde{V}_{i,p} - V_{i,p}\right)} \\ \text{with respect to} \quad & \boldsymbol{V_p} \\ \text{subject to} \quad & \text{design guidelines constraints,} \end{aligned} \tag{2}$$

where N_{lam} is the number of laminates in each structural part p. Accordingly, $\widetilde{\boldsymbol{V_p}}$ is the vector of input lamination parameters obtained from Proteus and $\boldsymbol{V_p}$ is the vector of lamination parameters retrieved by the optimization algorithm. The same Matlab routine takes care of handling the new set of lamination parameters such that the old Proteus model is updated properly.

Once a set of blended and thus manufacturable laminates are obtained, the medium-fidelity Nastran aeroelastic model can be generated. Another Matlab routine is employed to handle the geometrical and structural properties of the different structural parts and to build a shell model of the wing. The generated structural model includes spar flanges and ribs, which were not modelled in Proteus (the former not at all, the latter only with added masses). Every input to the MATLAB routine is taken from the manufacturable Proteus model, except for the flange width which has to be specified by the user. Aeroelastic analyses are carried out on the Nastran model for the same load cases used in Proteus optimization.

The results of the aeroelastic analyses allow a reliable assessment of skin buckling and spar flange crippling. Crippling is a stability failure where a flange buckles locally under compressive load, with the half-wavelength of the buckled flange being much smaller than the length of the main structural element [24]. Here the crippling of both spar flange and web is assessed, using the design equation for One-Edge-Free (OEF) crippling for the former:

$$\begin{cases} \dfrac{\sigma_{crip}}{\sigma_c^u} = 1 & \text{for } b < 1.98t \\[2ex] \dfrac{\sigma_{crip}}{\sigma_c^u} = \dfrac{1.63}{\left(\dfrac{b}{t}\right)^{0.717}} & \text{for } b \geq 1.98t, \end{cases} \tag{3}$$

and the design equation for No-Edge-Free (NEF) crippling for the latter [24]:

$$\begin{cases} \dfrac{\sigma_{crip}}{\sigma_c^u} = 1 & \text{for } b < 8.443t \\[2ex] \dfrac{\sigma_{crip}}{\sigma_c^u} = \dfrac{11.0}{\left(\dfrac{b}{t}\right)^{1.124}} & \text{for } b \geq 8.443t, \end{cases} \tag{4}$$

where σ_{crip} is the crippling stress, σ_c^u is the ultimate compressive strength of the flange, b is the flange width and t is the flange thickness. If the compressive stress in the flange is smaller than the crippling stress, then the flange is not supposed to undergo crippling failure.

When the flange is found to be critical in crippling, a new flange width is chosen. Taking a smaller width is the logical choice, as the crippling stress becomes larger in this way. However, this entails making the skin panels more prone to buckling, since the respective panel area is enlarged[†]. Besides, reducing the flange width also reduces the area of the bonding surface between the spar and the two skins. Due to these reasons and due to the manufacturability

---

[†] A skin buckling panel is delimited by the structural elements of the internal structures, that is to say spars and ribs. The spar flanges are supposed to be attached to the two skins, thus stiffening the part of the skin panel where a spar flange is present. In this way the area of the skin panels most prone to buckling is limited to the part where the spar flanges are absent. When the width of the flange is reduced, the area most prone to buckling enlarges and thus the buckling load of the skin panel decreases.

constraint, the flange width cannot be arbitrarily reduced and a trade off must be found. Increasing the flange thickness can be helpful in terms of crippling, however that cannot be arbitrarily chosen as it corresponds to the overall spar thickness, which in turn is a result of Proteus optimization (unless the thickness is kept constant and only the stiffness is optimized). The Nastran model is regenerated with the new flange width and both buckling and crippling are assessed again. This operation is repeated until a safe flange width is established.

Once the flange width is chosen, the Nastran model is used for the correction of the optimization constraints used in Proteus. The strain and buckling constraints are set as:

$$\begin{cases} h_s < \dfrac{1}{1.5 \cdot k_s} \\ \\ h_b < \dfrac{1}{1.5 \cdot k_b}, \end{cases} \tag{5}$$

where k_s and k_b are correction coefficients. The correction coefficient for strain, k_s, is found considering the maximum absolute values of principal strains and maximum shear for one selected load case from both Nastran and Proteus results:

$$\begin{gathered} \max\left|\epsilon_{max,nastran}\right|, \max\left|\epsilon_{min,nastran}\right|, \max\left|\gamma_{max,nastran}\right|, \\ \max\left|\epsilon_{max,proteus}\right|, \max\left|\epsilon_{min,proteus}\right|, \max\left|\gamma_{max,proteus}\right|. \end{gathered} \tag{6}$$

Subsequently, the ratio between Nastran and Proteus values is calculated and the highest value among these ratios is taken as the correction coefficient:

$$k_s = \max\left(\frac{\max\left|\epsilon_{max,nastran}\right|}{\max\left|\epsilon_{max,proteus}\right|}, \frac{\max\left|\epsilon_{min,nastran}\right|}{\max\left|\epsilon_{min,proteus}\right|}, \frac{\max\left|\gamma_{max,nastran}\right|}{\max\left|\gamma_{max,proteus}\right|}\right) \tag{7}$$

For the same load case the highest buckling index found in Nastran is compared to the buckling index obtained in Proteus for the same panel. k_b is taken as the ratio between Nastran and Proteus indices.

The optimization is re-run with the corrected optimization constraints and the process follows as described previously. Once the design is proven buckling and crippling free with Nastran it is considered finalized.

C. Tools Interface

1. Proteus - OptiBLESS - Proteus

As mentioned in Section III.B, a Matlab routine is developed to feed OptiBLESS with the lamination parameters of the optimized Proteus model and to update the latter with the new lamination parameters. The Matlab routine is called `Proteus2Optibless.m` and its flow diagram is shown in Fig. 2.

First, the optimization results are loaded. In this way the vector including the optimal design variables is retrieved together with the IDs used to identify the laminates in Proteus. This data is used to give the right input to OptiBLESS. The latter can find a blended stacking sequence of a laminated structure formed by different patches, where a patch is defined as a region where the stacking sequence is uniform. Thus a structural part, that is to say bottom skin, top skin or spars, correspond to a laminated structure of OptiBLESS and Proteus' laminates corresponds to OptiBLESS' patches. For this reason, the retrieved IDs are used to group together the laminates belonging to the same structural part, and in this way lamination parameters and thicknesses are distinguished for each laminated structure that has to be fed into OptiBLESS. At this point a loop is run through the different laminated structures defined in the previous operation and OptiBLESS is called each time. The inputs given for each laminated structure are constituted by a set of laminate (patch) numbers, a set of lamination parameters to be matched and the bounds for the number of plies to be used. To establish the last input, the optimal laminate thicknesses obtained by Proteus have to be coupled with a ply thickness specified by the user. At the end of the loop, each laminate structure has a set of blended stacking sequences and thus a certain number of plies for each patch. The last operation performed by `Proteus2Optibless.m` is to update the design variables of the Proteus model with the new lamination parameters and thicknesses.

2. Proteus - MSC Nastran

The generation of the Nastran model from the Proteus model is carried out by means of the Matlab routine `Proteus2Nastran.m`. This routine makes use of a purpose-developed object-oriented framework to handle the

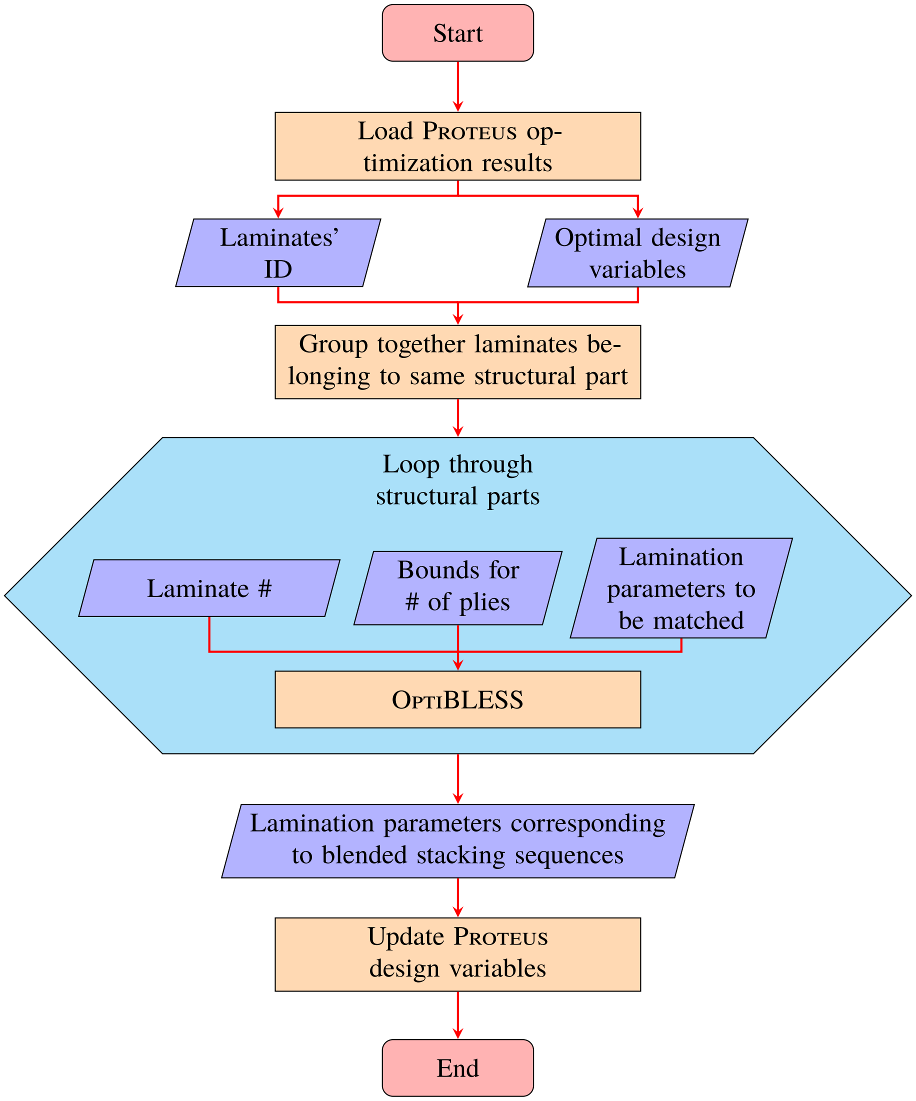

Fig. 2 Flow diagram of `Proteus2Optibless.m`.

Nastran-related data. The structure of such framework is shown in Fig. 3.

The top element in the hierarchy of the object-oriented framework is the `NastranAnalysis` object. This contains everything needed to run analyses and to process the results: the `NastranExecutiveControl` object, where the solution sequence is specified, the `NastranCaseControl` object, where the subcases of the nastran analysis are defined, the `NastranSubcaseResult` object array, where the results are stored and the `NastranBulkData` object, where the numerical aeroelastic model is defined.

The two main children of `NastranBulkData` object are an array of `Grid` objects and an array of `NastranPart` objects. The `Grid` objects define all the structural nodes of the numerical model, while the array of `NastranPart` objects defines the different structural parts, such as bottom skin, top skin, spars and ribs. A `NastranPart` object, in turn, contains a name, needed for identification, and an array of `NastranRegion` objects. These correspond to laminate definitions in Proteus, namely a part of the structure with same structural properties, defined by lamination parameters and thickness. Thus a `NastranPart` object may contain several `NastranRegion` objects since a structural part in Proteus may be composed by several spanwise laminates.

The three main components of a `NastranRegion` object are the element array, the element property and the material property. The first component includes `Cquad4` and `Ctria3` objects that correspond to the analogous Nastran cards and that are used to define the quadrilateral and triangular shell elements of the structural model. Quadrilateral elements are used throughout the entire model, while triangular elements are only used at the leading and trailing edge of the ribs. The `Cquad4` and `Ctria3` objects are linked to the elements of the `Grid` object array that form each shell element. The element property contains a `Pshell` object, which defines the membrane, bending and transverse shear properties of all shell elements belonging to the `NastranRegion` object. Finally, the material property is defined by an array of `Mat2` objects, which are used to define the thickness-normalized $\hat{\boldsymbol{A}}$ and $\hat{\boldsymbol{D}}$ matrices [25]:

$$\hat{\boldsymbol{A}} = \boldsymbol{A}\frac{1}{t}, \qquad \hat{\boldsymbol{D}} = \boldsymbol{D}\frac{1}{t}. \tag{8}$$

It should be noticed that the definition of element array, element property and material property as children of the `NastranRegion` object facilitates the assignment of structural properties to shell elements, since each knows what `Pshell` object it is linked to through the common parent `NastranRegion`. The last two components of a `NastranRegion` object are the subregion array and the overlay region array. These are in turn array of `NastranRegion` objects. The subregion array is used to define subsections within a region, while the overlay region is used to link another region sharing the same structural nodes but having different structural properties. The employment of these two features will be explained in more detail later.

A representation of the flow diagram of `Proteus2Nastran.m` is given in Fig. 4. The routine starts with loading the PROTEUS model and the settings for the generation of the NASTRAN model. The loaded data is used to initialize the `NastranBulkData` object. All `NastranPart` and `NastranRegion` objects are generated, together with all element and material properties. In order to model the spar flanges, subregions and overlay regions are also initialized in this phase. Spar flanges are modelled by defining additional shell elements on top of those defined for the skins, using the same structural nodes. The centre-plane of shell elements belonging to flanges is shifted vertically to account for skin and flange thicknesses. Subregions and overlay regions are then used to identify the part of the laminate where a skin intersects a flange and to indicate the link between the two.

Once the `NastranBulkData` object is initialized, the structural mesh can be generated. This step involves the actual generation of structural nodes and shell elements. This is carried out one patch at a time, where a patch is defined as a portion of a region enclosed by the intersections with other regions. An example can be a portion of wing skin delimited by the intersections with the edges of two ribs and two flanges. In this way the junctions of different structural parts (such as skin-rib, spar-rib, etc.) are discretized coherently. Subsequently, the boundary conditions are applied using a `Spc1` card, which clamps the wing at the root. Additional concentrated masses present in PROTEUS are included in the model with `Conm2` cards in a similar way as discussed by Dillinger [25].

The next step consists in the generation of the aerodynamic mesh and of the aeroelastic coupling. DLM is used as aerodynamic method, which requires the discretization of the wing into flat trapezoidal panels that are in turn subdivided in a certain number of boxes according the desired mesh size. This discretization is linked to the wing planform definition given in the PROTEUS model. The structural nodes are linked to the aerodynamic grid points by means of a surface spline in an analogous way as demonstrated in [25]. A load reference axis (LRA) is generated by placing auxiliary nodes at the centroid of each rib. In this way, the LRA constitutes a virtual axis along the spanwise direction employed to smoothly interpolate the loads from the aerodynamic elements to the structural nodes. Each auxiliary node of the LRA is connected by means of `Rbe2` rigid elements to other auxiliary nodes defined at the leading and trailing edge. The aerodynamic load is then interpolated on the LRA and on the rigidly connected nodes by means of `Spline1` cards. The nodes on the LRA are connected with `Rbe3` multi point connections to the nodes on the corresponding ribs' edge such that the forces can be transferred to the structural model and the LRA can follow the structural deformation.

The `Proteus2Nastran.m` routine terminates with the application of the same load cases used in PROTEUS, the generation of `NastranExecutiveControl` and `NastranCaseControl` objects and finally with the assembly of the `NastranAnalysis` object. The solution sequences 144 and 146 are set up for static and gust load cases, respectively. Once the `NastranAnalysis` object has been generated, the desired analyses can be run and the results post-processed to perform the crippling assessment and the correction of the optimization constraints.

IV. Optimization Setup

The proposed design framework is applied to the design of an aeroelastically tailored experimental wing. Therefore, it is necessary to define the optimization problem which constitutes the starting point of the framework.

As described in Section III.B, several inputs are needed for PROTEUS optimization. First, the wing geometry must be defined in terms of planform and airfoil distribution. A rectangular wing is chosen and a summary of its properties is reported in Table 1. Two spars are chosen for the structural layout of the wing. Their location along the chord is defined

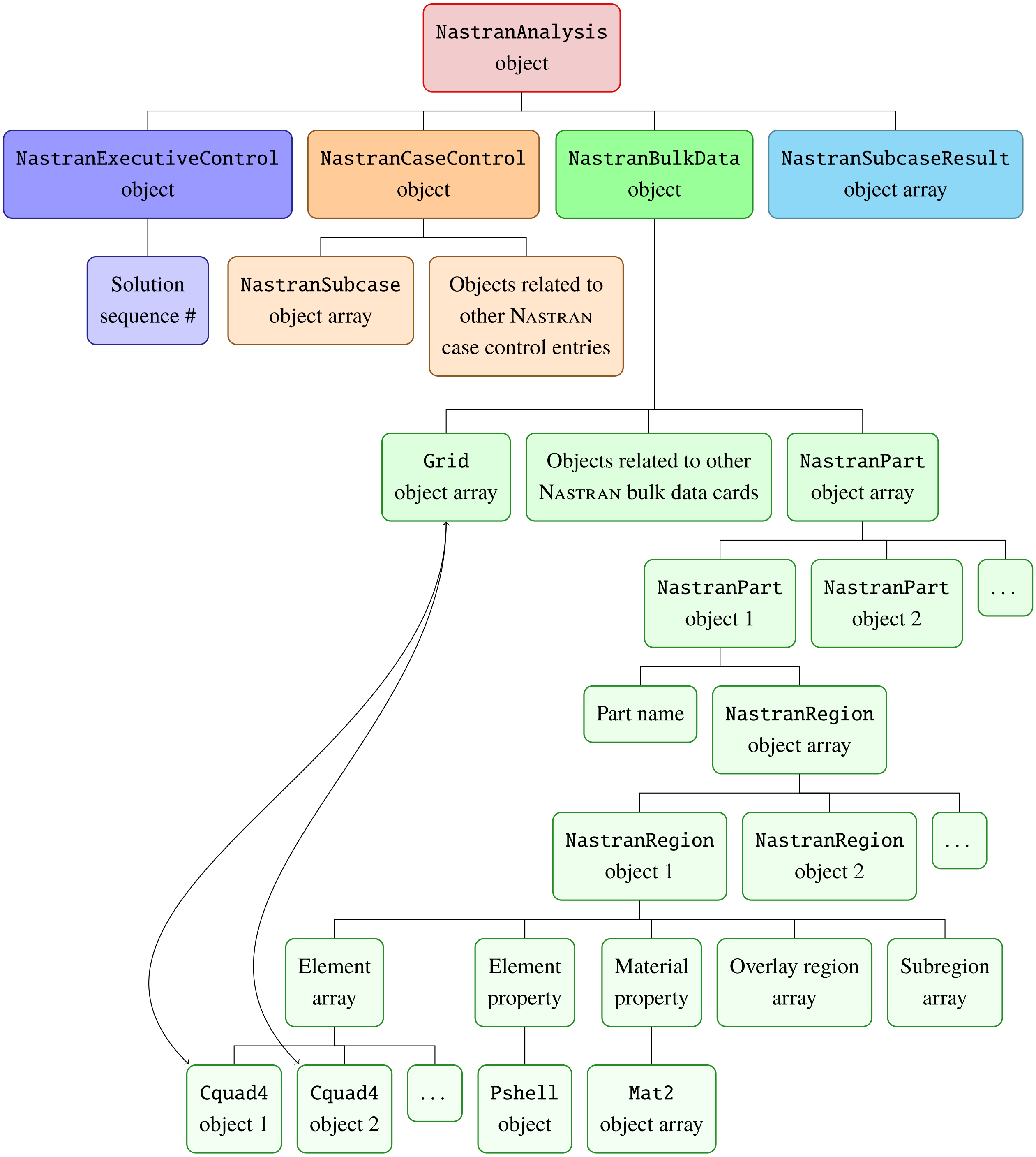

Fig. 3 Hierarchy of MATLAB objects used to generate the NASTRAN model.

in order to guarantee a web height of at least 1.5 cm, taking also into account the maximum allowed thickness of bottom and top skins.

After defining planform and spar locations, the number of ribs and their location are chosen. A total of 13 ribs are used, distributing them from wing root to tip and using a sine spacing to determine the distance between them. The purpose of such spacing is to cluster the ribs closer together at the root where the skin panels are more prone to buckling. This is caused by the reduction of the buckling load as the skin panel becomes larger, for same thickness and stiffness

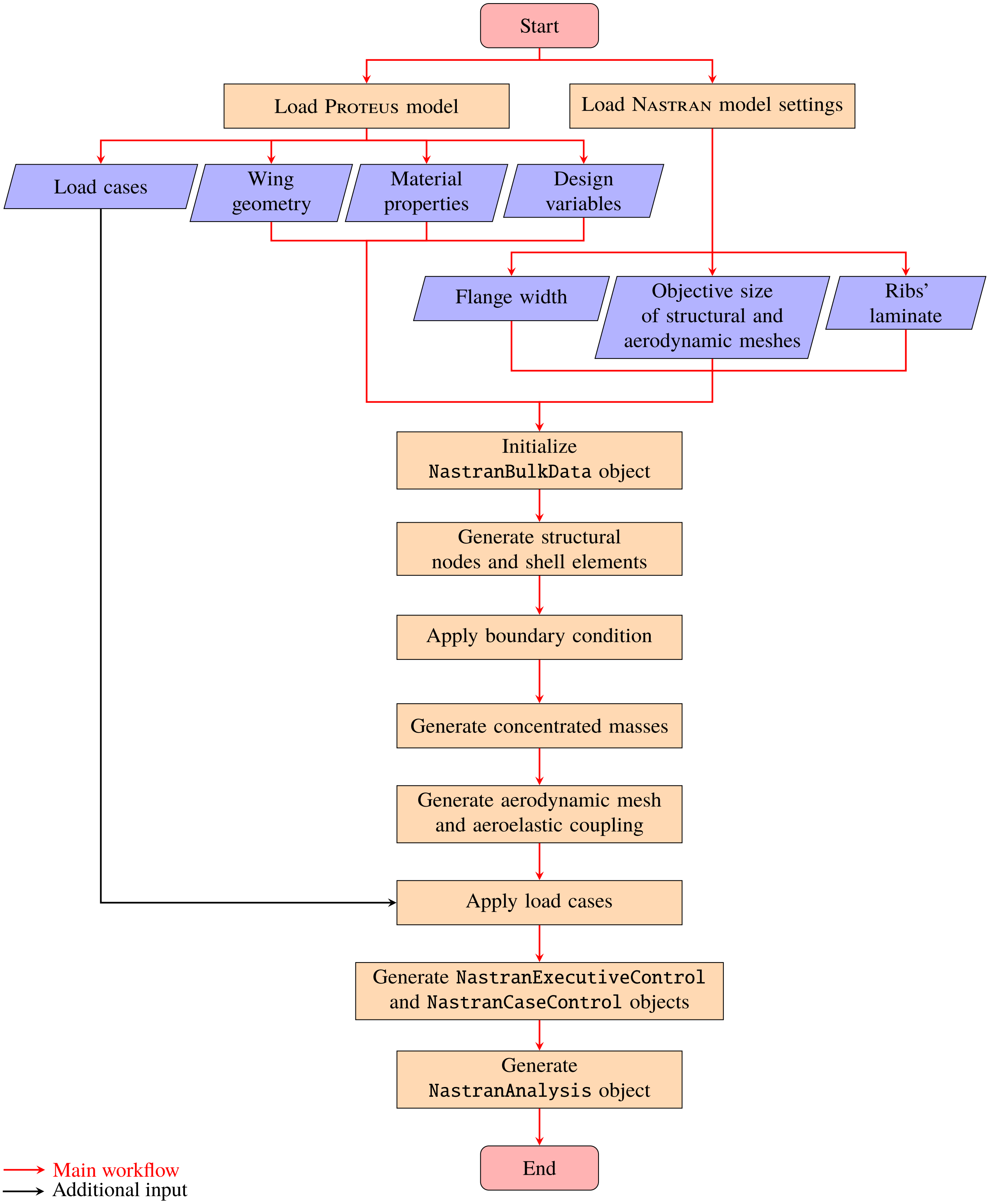

Fig. 4 Flow diagram of `Proteus2Nastran.m`.

properties. The last two ribs at the wing tip are placed at a distance of 3 cm, to form a housing space for a tip mass. The optimization is run considering a tip mass of 0.4 kg. This choice is made in order to lower the first eigenfrequency of

Table 1 Wing geometry.

Parameter	Value
Semispan, m	1.75
Chord, m	0.25
Front spar location, % chord	25
Rear spar location, % chord	65
Aspect ratio	14
Sweep angle, deg	0
Taper ratio	1
Airfoil	NACA 0010

the optimized wing. This is in turn desired so that the first eigenfrequency is of the same order of magnitude of the gust frequencies achievable with the gust generator during the experimental campaign. Both ribs and tip mass are modelled as lumped mass and no additional stiffness is considered for the ribs.

In order to define the design variables of the optimization, the wing has to be divided into a certain number of design regions. Within each design region, a laminate is defined for each structural part so that the wing is partitioned in a total of $n \cdot m$ laminates, where n is the number of design regions and m is the number of structural parts (4 in case of top skin, bottom skin and two spars). As mentioned in Section III.B, each laminate has constant properties described by its thickness and by 8 lamination parameters. For the present case, the wing is divided in 3 design regions, leading to a total of 108 design variables. However, the two spars are represented with a single laminate and their thickness is defined ab initio to be 0.524, corresponding to four plies, which is not further optimized. This choice is made for ease of manufacturing and to reduce the complexity of the crippling assessment. Consequently, the number of active design variables is reduced to 70. An overview of the design regions together with the layout of the spars and ribs is given in Figure 5.

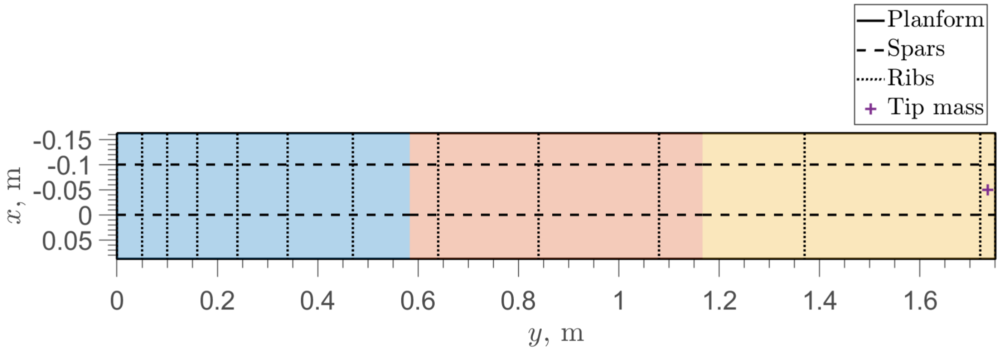

Fig. 5 Wing planform with layout of spars, ribs and tip mass. The different colors indicate the design regions.

The carbon-fibre-epoxy unidirectional prepreg Hexcel 8552 IM7 [26] is selected for the manufacturing of the wing. The corresponding properties are thus chosen for the definition of the material properties in Proteus, which are given in Table 2.

The remaining inputs for the optimization are the objective function and the load cases. The objective function is defined by a combination of wing weight minimization and wing tip displacement maximization for the first load case. Since the wing has to be tested in a wind-tunnel environment, the load cases are defined in terms of static angle of attack with the aim of mimicking the usual $1g$, $2.5g$ and $-1g$ load conditions. Besides, given that dynamic wind-tunnel tests are envisioned by means of the gust generator available at TUD, a critical gust assessment is performed for the first load case [27]. This means that on top of the static load, the effect of several 1-cosine gusts on the wing is assessed. The

Table 2 Material properties used in the optimization [26].

Property	Value
E_{11}, GPa	148.3
E_{22}, GPa	9.3
G_{12}, Gpa	4.68
ν_{12}	0.32
ρ, kg/m^3	1570
X_t, Mpa	2500
X_c, Mpa	1716
Y_t, Mpa	64
Y_c, Mpa	285.7
S, Mpa	91.15
t_{ply}, mm	0.131

range of gust frequencies used for the assessment varies from 0.6 Hz to 5 Hz, while the incremental angle of attack generated by the gust is chosen as $\Delta\alpha_g = 5$ deg. A summary of the load cases is given in Table 3.

Table 3 Optimization load cases

Load case #	Angle of attack, deg	Flight speed, m/s	Critical gust assessment
1	3	28	Yes
2	7.5	28	No
3	-3	28	No

The choice of including wing tip displacement maximization in the optimization objective is related to the requirement that the design is fatigue critical, which is assessed by means of the method presented in [28]. However, since the focus of this paper is only on the application of the presented design framework, no additional detail related to the fatigue of the wing is discussed. Finally, a further specification of the optimization parameters is given in the Appendix.

V. Numerical Results

In this section the results of the application of the design framework to the case described in Section IV are presented, with focus on the comparison between optimum and manufacturable designs and on the assessment of buckling and crippling. Only the results from the final loop of the design process are discussed for the sake of conciseness.

The optimization problem set up in Section IV is run within Proteus and subsequently blended stacking sequences of the optimized laminates are retrieved with OptiBLESS. The resulting stacking sequences of top and bottom skins are given in Table 4. It can be noticed how the presence of tip displacement maximization in the optimization objective drives the stiffness to be primarily directed away from the spanwise direction as almost all ply angles are closer to ±90 degrees rather than to 0.

The use of OptiBLESS to retrieve blended stacking sequences inevitably affects the thickness and stiffness of the laminates. The effect on the former can be observed in Figure 6. The only laminate undergoing a change in laminate thickness smaller than 5% is the one corresponding to the first design region of the top skin. All the other laminates experience moderate to large changes in thickness, caused by the fact that the blended laminate thickness is constrained to a multiple of the ply thickness. Moreover, it can be observed that in most cases the blended laminates result thinner than the optimal laminates. The reason for this is twofold. First, the result of the optimization performed in OptiBLESS is influenced by the bounds set in terms of number of plies. In the present case, the manufacturable design was required

Table 4 Stacking sequence table of top skin, bottom skin and spars, ply angles in degrees.

Top skin			Bottom skin			Spars		
Design region #			Design region #			Design region #		
1	2	3	1	2	3	1	2	3
55	55	55	−75	−75	−75	70	70	70
−65	−65		50			−60	−60	−60
75			−30			−60	−60	−60
−70	−70	−70	55	55	55	70	70	70
75			−30					
−65	−65		50					
55	55	55	−75	−75	−75			

to be not more conservative with respect to the Proteus optimization result. The bounds in terms of number of plies are then selected accordingly. Furthermore, the simultaneous symmetry and blending constraints on the laminates forces to remove always an even number of plies at the ply drops. Given the relatively small maximum number of plies possible, the outboard laminates are more likely to get thinner as a result of OptiBLESS optimization.

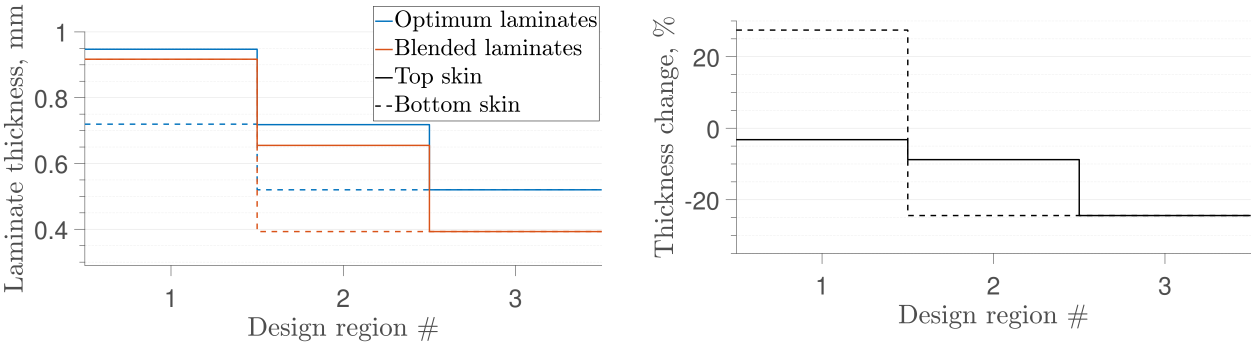

(a) Laminates' thickness.

(b) Change in laminates' thickness.

Fig. 6 Comparison between the thickness of optimum and blended laminates.

As far as the change in stiffness is concerned, Figure 7 shows a comparison between the stiffness polar of the optimum and of the blended laminates. As already noticed with the stacking sequence table, the stiffness is mainly directed away from the span axis, both for the optimum and the blended laminates and especially considering the membrane stiffness. However, substantial differences can be observed between the stiffness of the optimum and the blended laminates. Only the membrane stiffnesses of the first design region of both skins are well matched and the quality of the match deteriorates progressively in the subsequent design regions. This is an inevitable consequence of the blending requirement combined with the relative small number of available plies. In fact, the laminate of the first design region of each skin is the thickest and this gives to the optimizer used in OptiBLESS a design space large enough to match the optimum stiffness finely. However, when switching to the laminate of the adjacent patch, the design space is reduced both by the need to continue some plies from the previous patch and by the presence of less plies. This makes the matching of both membrane and bending stiffnesses over the entire skins very challenging.

The change in laminate thickness resulting from the blended stacking sequence retrieval influences the buckling indices of the two skins. Figure 8a and Figure 8b show the augmented buckling indices resulting from load case #2 for optimal and blended top skin, respectively, where the augmented buckling index is defined as the buckling index multiplied by the safety factor 1.5 and the correction factor k_b: $h_b \cdot 1.5 \cdot k_b$. For the final loop of the design process, a correction coefficient $k_b = 0.35$ is used for buckling. In the figures it can be observed how the buckling indices are generally larger in the manufacturable design (where laminates are obtained from OptiBLESS) with respect to the

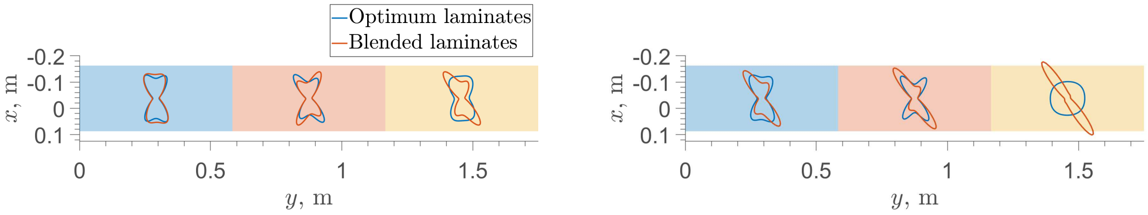

(a) Top skin membrane stiffness. **(b) Top skin bending stiffness.**

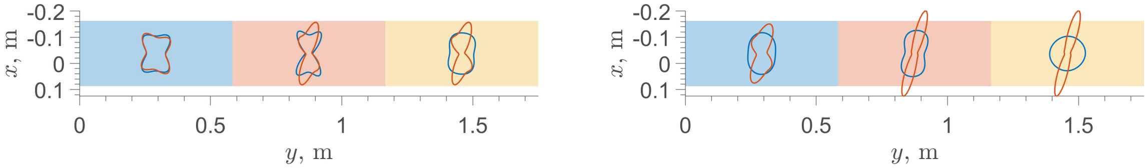

(c) Bottom skin membrane stiffness. **(d) Bottom skin bending stiffness.**

Fig. 7 Comparison between the stiffness of optimum and blended laminates.

optimum design (where the laminates are obtained from Proteus optimization), which is a consequence of the laminate thickness reduction observed in Figure 6b.

The augmented buckling indices of the central buckling panels of the wing (the ones corresponding to the wingbox) and their change are reported in Table 5. It is important to notice that the augmented buckling indices of the blended skin resulting larger than 1 are not indicative of the actual buckling behaviour of the skin panels. In fact, those indices include the factor k_b, which is derived in the previous iteration of the design process. This factor is design-dependent, since it is obtained from the ratio between the most critical buckling index resulting from Nastran and the buckling index of the corresponding panel of the blended Proteus model. When a new optimization is run and the new blended laminates are obtained, the critical buckling panel can change, making the correction coefficient k_b from the old iteration inadequate to indicate the critical buckling panel within Proteus analysis. The Nastran model is indeed needed to verify that the new design is buckling free.

From Table 5 it can be noticed how the most critical panel in the optimal design is the one closest to the root of the wing, while in the manufacturable design the most critical panel becomes the 10th along the span. However, when the Nastran model is generated (introducing the spar flanges) and analysed for the same load case, the first buckling mode of the wing results to be associated with 7th panel, as it can be observed in Figure 8c. Besides, the buckling index predicted for such panel is approximately equal to 0.52, becoming 0.79 if multiplied by the safety factor 1.5. This means that the manufacturable wing model including spar flanges is buckling free for the considered load case, with the flange width used for the final design loop being equal to 2 cm.

Nastran is also used to assess the crippling of spars. Equations (3) and (4) are used to evaluate the crippling stress ratio σ_{crip}/σ_c^u. The resulting curves describing the behaviour of the crippling stress ratio are shown in Figure 9. The points corresponding to the flange and the two webs of the final design are indicated. Only those three points are indicated because the two spars have same and constant thickness, the flange width is the same for both spars and the only difference in terms of the ratio b/t is given by the different heights of the two spars[‡]. It can be observed how the potentially most critical element is the spar flange, having a lower crippling stress ratio with respect to the two webs. However, this also depends on the stress level on flanges and webs. In fact if for the considered load case one of the flanges' shell elements undergoes the largest compressive stress over the internal structure, then the flange is indeed more prone to crippling with respect to the webs. In that case, only the crippling stress of the flange has to be calculated and compared with the largest compressive stress acting on the flange. Otherwise, if one of the two webs' shell elements undergoes the largest compressive stress, then the crippling stress must be calculated for both flange and webs and compared with the respective largest compressive stress.

The ultimate compressive strength σ_c^u of the laminate is obtained using the maximum stress failure theory, taking

---

[‡] For the crippling assessment, the height of the web corresponds to what is typically referred as width for flanges.

Table 5 Augmented buckling indices ($h_b \cdot 1.5 \cdot k_b$) of central buckling panels of optimum and blended top skin. Buckling panels are counted from root to tip of the wing.

Buckling panel #	Augmented buckling index		Difference, %
	Optimal top skin	Blended top skin	
1	0.87	1.00	15.50
2	0.81	0.94	15.48
3	0.81	0.94	15.75
4	0.75	0.87	16.76
5	0.63	0.74	17.91
6	0.59	0.69	17.62
7	0.46	0.55	18.42
8	0.77	1.39	79.18
9	0.50	0.91	82.24
10	0.48	2.38	398.97
11	0.19	1.03	441.83
12	0.00	0.01	563.64

into account the typical knockdown factors accounting for adverse environmental effects and damage[§] [24]. The crippling stress of the flange and the two webs is then found using the points in Figure 9. Finally, this value is compared to the compressive stress in a selected CQUAD4 elements of flange and webs. The element is chosen from the NASTRAN results of load case #2. For such load case, the element undergoing the largest compressive stress along the spanwise direction is found, where the spanwise direction corresponds to the x-axis of the elements' coordinate system. The resulting crippling stress is multiplied by a safety factor of 1.5, for consistency with previous safety criteria. An example of stresses in the wing's internal structure (spars and ribs) calculated by NASTRAN is given in Figure 10, where the normal stress along the spanwise direction is shown. As it can be observed, the element with the largest compressive stress is located at the root of the front spar flange. This means that flange is the most critical part for crippling, and thus the webs can be disregarded from the assessment. The value of compressive stress found in the `Cquad4` element is compared with σ_c^u and σ_{crip} in Table 6, where it can be noticed how the final design results crippling free for load case #2.

Table 6 Comparison between ultimate compressive strength of spar laminate, crippling stress and compressive stress resulting from NASTRAN for load case #2. Stresses in MPa.

σ_c^u	σ_{crip}	$\sigma_{c,nastran} \cdot 1.5$
−420.2	−50.3	−38.4

VI. Manufacturing and Experimental Results

The optimized wing is manufactured in the Delft Aerospace Structures and Materials Laboratory (DASML). The wing is manufactured as part of a larger project ongoing at TUD. The focus of the project is the effect of fatigue on the aeroelastic design of a wing [28]. Manufacturing of the wing is briefly presented here, for the sake of completeness. The experimental wing is manufactured with a span of 1.8 m, extending the root of the wing for 5 cm with respect to the nominal span of 1.75 m. This is done in order to include an aluminium block inside the first 5 cm of the wingbox

---

[§] Material scatter is already taken into account in the formulation of Eq. (3) and (4).

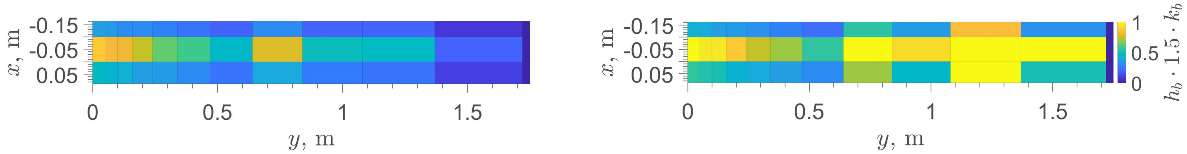

(a) Optimal top skin buckling index.

(b) Blended top skin buckling index.

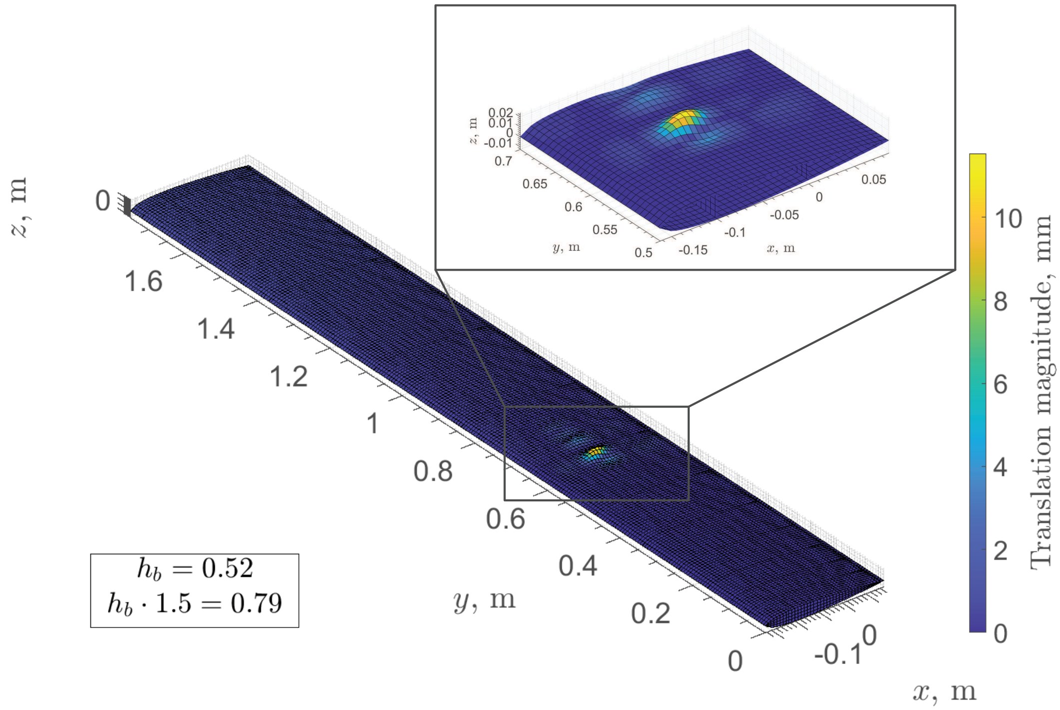

(c) First buckling mode of wing with blended laminates and flange size of 2 cm predicted by NASTRAN.

Fig. 8 Comparison between the buckling indices of optimal and blended skins for load case #2.

section, thus facilitating the clamping mechanism of the wing. Furthermore, an additional part called leading edge strip is fabricated using a $[45, -45]_s$ laminate. This part is placed along the leading edge of the wing and provides a 1 cm wide connection area for top and bottom skin. The manufacturing steps are described in short below.

- An IM7/8552 UD prepreg roll is cut in patches according to the blended stacking sequences resulting from the design study and using a GERBER laminate cutting machine.
- Hand lay-up on aluminium molds of all optimized parts (top skin, bottom skin, front spar and rear spar) is performed in a clean-room using the prepreg patches previously prepared.
- Each component is vacuum bagged separately and cured in an autoclave.
- Each cured part is trimmed to the right dimensions.
- The ribs are cut from 3 mm quasi-isotropic carbon fibre plates acquired off the shelf[¶] using a CNC water-jet cutting machine.
- Front spar, rear spar and ribs are bonded together to form the internal structure of the wing's internal structure. An adhesive past Araldite AW 4858 is used for this and following bonding operations.
- The assembled inner-structure of the wing is bonded on the top skin, together with the leading edge strip and the aluminium block (see Fig. 11a).
- The wing is closed by placing the bottom skin on top of the other assembled parts and bonding those together (see Fig. 11b).

[¶] `http://www.carbonexperience.nl/index.php?route=product/product&path=24&product_id=359`, accessed: 24/11/2019.

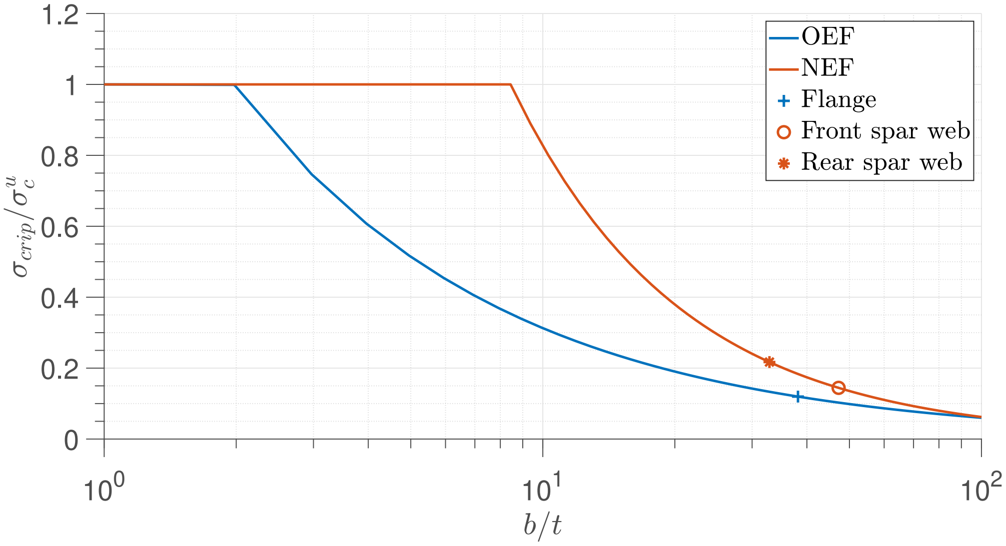

Fig. 9 **Crippling curves with points corresponding to the spar elements of the final design.**

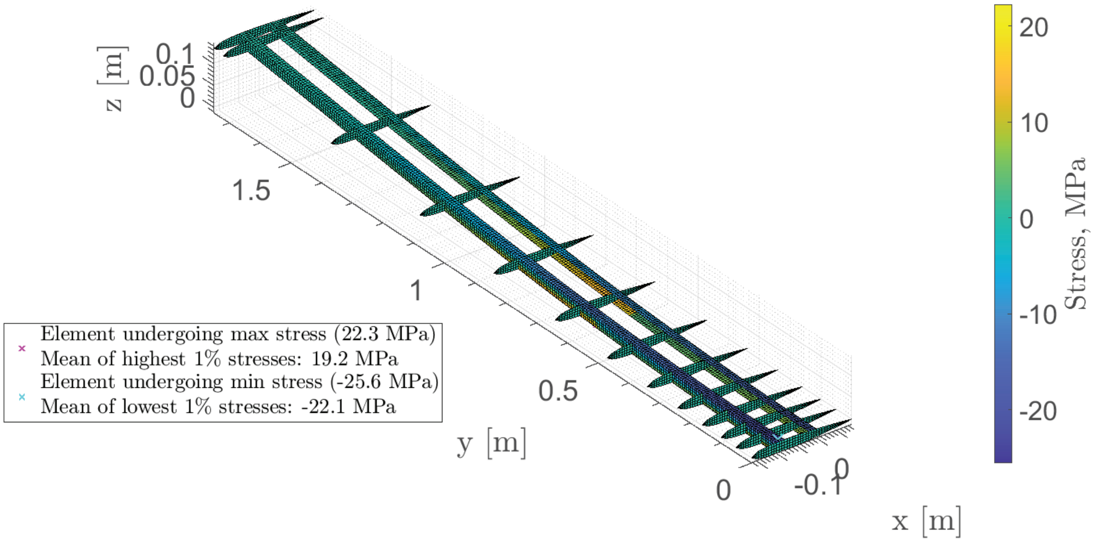

Fig. 10 **x-normal stresses of wing's internal structure (spars and ribs) in the `Cquad4` elements' reference frame for load case #2.**

An experimental campaign is conducted in the Open Jet Facility (OJF) at TUD in order to validate the employed design methodology. The OJF is a closed-loop, open test section wind-tunnel with an octagonal outlet section of 2.85×2.85 m^2 and a maximum achievable free-stream velocity of 35 m/s[‖]. The contraction ratio is 3 : 1 and the turbulence intensity is reported to be lower than 0.5% at 1 m from the tunnel nozzle [29]. The wind-tunnel is equipped with a gust generator in order to provide dynamic excitation during the tests [30, 31].

The experimental setup is shown in Figure 12. The gust generator is installed in front of the outlet section of the wind-tunnel. Two measurement systems are used: a 6-component balance for overall forces and moments and a scanning vibrometer (*Polytec PSV-500 Scanning Vibrometer*[**]) for displacements. Vibrational displacement and acceleration

---

[‖] `https://www.tudelft.nl/lr/organisatie/afdelingen/aerodynamics-wind-energy-flight-performance-and-propulsion/facilities/low-speed-wind-tunnels/open-jet-facility/`, accessed: 24/11/2019.

[**] The system used is a *PSV-500-B* with a *PSV-I-550 Scanning Head Xtra*. Specifications available at `https://www.polytec.com/fileadmin/d/Vibrometrie/OM_DS_PSV-500-1D_E_42445.pdf`, accessed: 24/11/2019.

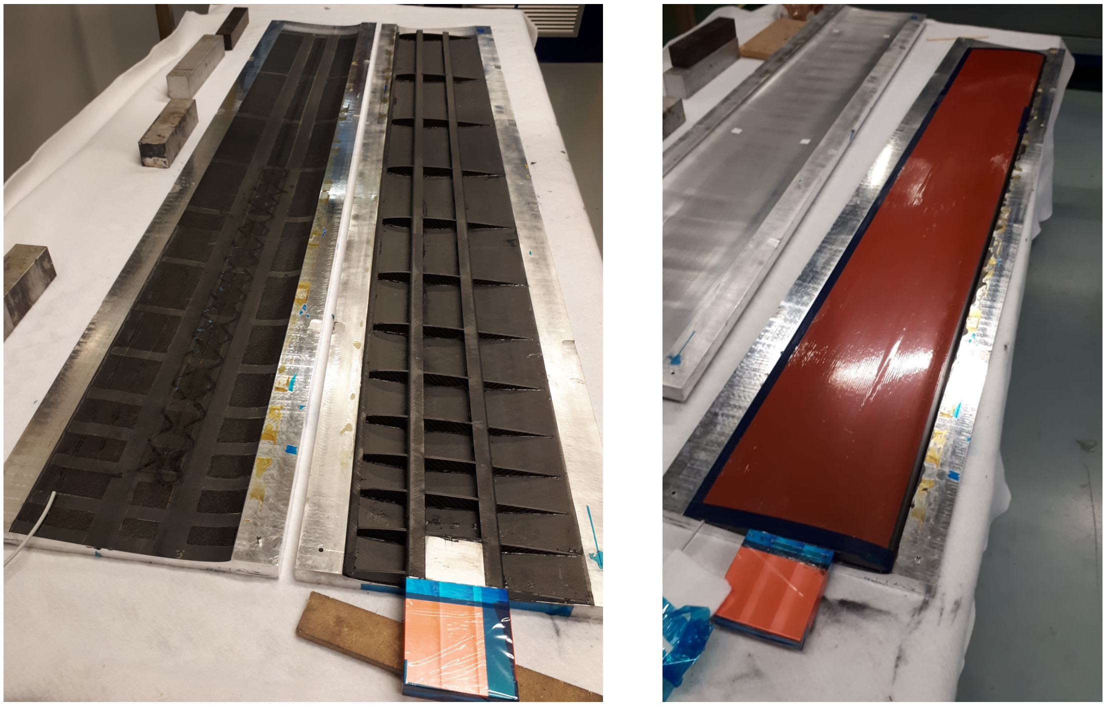

(a) Two halves of the wing before final bonding. **(b) Assembled wing after final bonding.**

Fig. 11 Final phases of wing manufacturing.

can also be obtained by means of integration and differentiation of the measured vibration velocity, respectively. The resolution of the measured velocity is better than 14 μm/s.

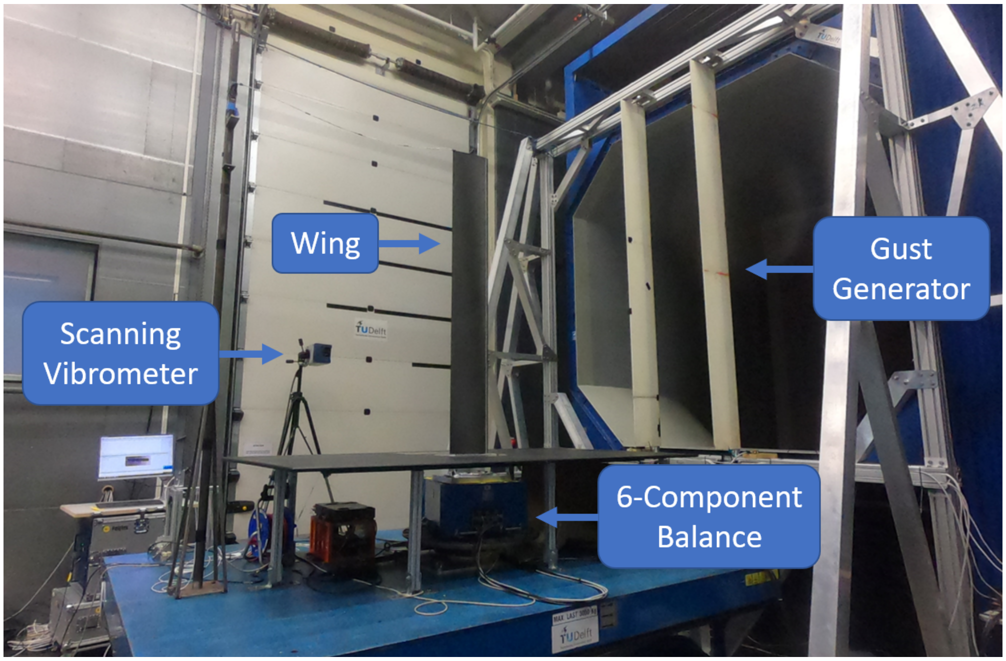

Fig. 12 Illustration of the experimental setup.

The wing is tested at various wind-tunnel velocities, static angles of attack, gust amplitudes and frequencies. A summary of the testing conditions is given in Table 7. As it can be noticed, the two wind-tunnel velocities used, 14 m/s and 25 m/s, are both lower than the velocity used for the optimization load cases. This is due to operational constraints on the wind-tunnel fan. The Reynolds numbers corresponding to the two velocities are $2.4 \cdot 10^5$ and $4.3 \cdot 10^5$, respectively. The wing is equipped with zig-zag tapes on pressure and suction side of the wing in order to force boundary layer transition from laminar to turbulent and in this way suppress any potential laminar separation bubble. A tape of 0.2 mm is applied on the suction side at 5% of the chord and a tape of 0.5 mm is applied on the pressure side at 65% of the chord. These values are selected according to the method presented in [32] and using airfoil pressure distributions predicted by Xfoil [33].

Table 7 Test matrix for the wind-tunnel experiment.

	Static test	Dynamic test
Wind-tunnel speed, m/s	14, 25	14, 25
Static angle of attack, deg	-1, 2, 4, 6, 8, 10	4
Gust frequency, Hz	–	2, 4, 8
Gust vanes angle, deg	–	5, 10

The static wing polar at 25 m/s is presented in Fig. 13 in terms of lift coefficient and bending moment coefficient[††]. The experimental data is compared with the predictions of Proteus and Nastran. In the figure the effective angle of attack is used instead of the nominal ones given in Table 7, since during the tests the angles of attack were set based on the reference frame of the turn-table used to rotate the balance-wing system. Afterwards the angle of attack giving zero lift was found to be 0.58°. Therefore the nominal angle of attack was corrected for this offset when comparing to the numerical results. These show almost identical lift curves for Proteus and Nastran models, with both overestimating the lift slope (see Fig. 13a). Also for the bending moment curve the two numerical models appear to provide almost identical results, except for the largest angles of attack, where Proteus follows better the experimental results (see Fig. 13b). A summary of the mean percentage errors of the numerical predictions with respect to the wind-tunnel results is given in Table 8. The mean percentage error is calculated as the average among the percentage errors of the numerical points with respect to the experimental points along the curve.

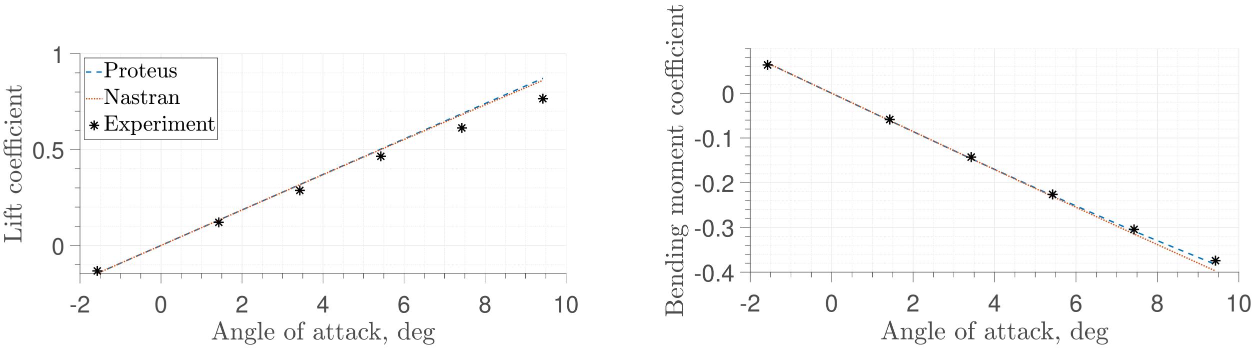

(a) Lift coefficient curve. **(b) Bending moment coefficient curve.**

Fig. 13 Results of static wind-tunnel tests at 25 m/s.

One reason for the observed errors can be ascribed to the aerodynamic modelling used in the numerical models. Both Proteus and Nastran use inviscid linear aerodynamic models, which are VLM and DLM respectively. The effect of using an inviscid model can be quantified comparing the lift curves resulting from viscous and inviscid Xfoil calculations for NACA 0010, as shown in Figure 14. For the viscous analysis, the wind-tunnel Reynolds number is set

---

[††] The sign of the bending moment coefficient is a consequence of the reference system used and of how the bending moment is calculated. The reference system employed has the x-axis aligned with the flow and the bending moment is considered as the reaction moment with respect to the x-axis at the constrained point.

Table 8 Mean and standard deviation of percentage error of numerical predictions with respect to wind-tunnel static test results. Results obtained considering tests at both 14 and 25 m/s.

	Proteus	Nastran
Error on lift coefficient, %	11.6 ± 4.3	8.9 ± 4.1
Error on bending moment coefficient, %	3.3 ± 3.8	2.1 ± 4.2

and forced transition is applied at the location of the zig-zag tapes. From the figure it is possible to notice how the slope of the inviscid lift curve is larger with respect to the slope of the viscous curve.

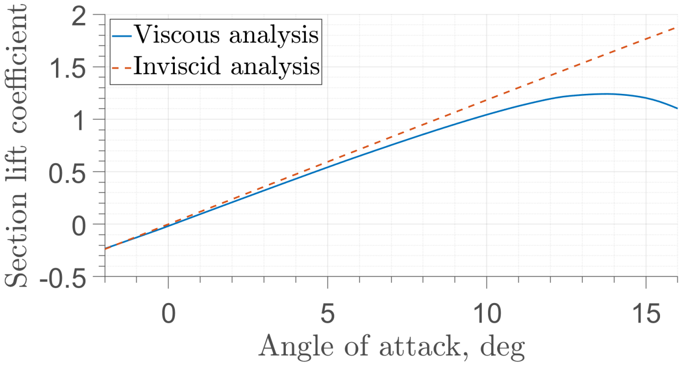

Fig. 14 Comparison of viscous and inviscid lift curve for a NACA 0010 resulting from Xfoil.

Dynamic tests are conducted for all the conditions indicated in Table 7 using 1-cosine gusts. The results are reported below, together with the comparison to the numerical predictions. For these, the gust incremental angle of attack $\Delta\alpha_g$ is obtained applying a correction factor of 0.48 to the gust vanes angle $\Delta\alpha_{gv}$, as indicated by the results of a previous study [31]. The gust speed V_g is then obtained through the relation $\tan\Delta\alpha_g = V_g/V_\infty$. In the current comparison, results are discussed in terms of incremental quantities with respect to the static condition before the action of the gust. The maximum incremental lift coefficient, bending moment coefficient and tip displacement are shown in Figure 15a, 15b and 15c, respectively. A summary of the mean percentage errors of the numerical predictions for the entire test matrix is given in Table 9. The source of these errors is believed to lie in the reason discussed earlier for the static results and in the gust correction factor, which depends on the distance of the wing from the gust generator, the speed of the wind tunnel and the frequency of the gust. A small change in either of these parameters can lead to a different correction factor. Nonetheless, the trend predicted by the numerical models agree with the experimental measurements in terms of critical gusts for force, moment and tip displacement.

Table 9 Mean and standard deviation of percentage error of numerical predictions with respect to wind-tunnel dynamic test results. Results obtained considering tests at both 14 and 25 m/s. For tip displacement, the points with $V_\infty = 25$ m/s, $\Delta\alpha_{gv} = 10$ deg and $f_g = 2, 4$ Hz are not considered.

	Proteus	Nastran
Error on lift coefficient increment, %	3.8 ± 11.4	−9.4 ± 20.4
Error on bending moment coefficient increment, %	−1.0 ± 7.5	−5.2 ± 21.3
Error on tip displacement increment, %	6.9 ± 5.2	−13.7 ± 18.3

Two points of Figure 15 are excluded from the error evaluation of tip displacement, namely the ones with velocity of 25 m/s, gust vanes angle of 10 deg and gust frequencies of 2 and 4 Hz. This is due to the fact that for these two conditions, the scanning vibrometer was not able to capture the large tip displacements, as the wing tip went out of

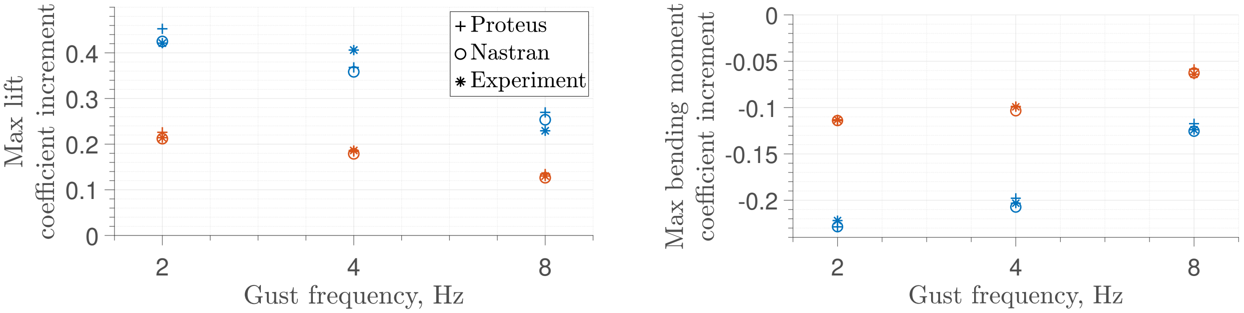

(a) Maximum incremental lift coefficient during gust.

(b) Maximum incremental bending moment coefficient during gust.

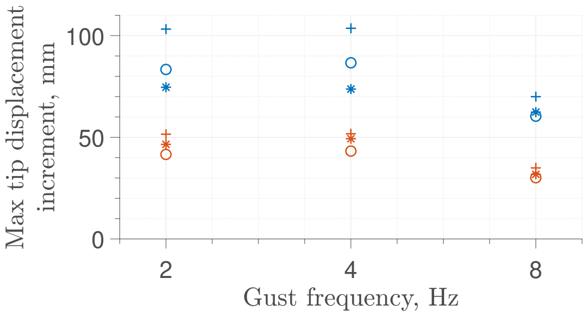

(c) Maximum incremental tip displacement during gust.

Fig. 15 Results of dynamic wind-tunnel tests at 25 m/s, gust vanes angle of 5 deg (orange) and 10 deg (blue).

the field of view of the instrument. This is observable in Figure 16, where the time history of the tip displacement for gust frequencies of 4 and 8 Hz with free-stream velocity of 25 m/s and gust vanes angle of 10 deg is plotted. For both frequencies the experimental curve appears to be halfway between the Proteus and the Nastran curve, both in terms of amplitude and frequency of the response. However, for the case with a gust frequency of 4 Hz, there is a loss of information due to the wing tip moving out the field of view of the scanning vibrometer, resulting in a flat line. Nevertheless, following the curvature of the response, the experimental curve would still be bounded between the numerical curves.

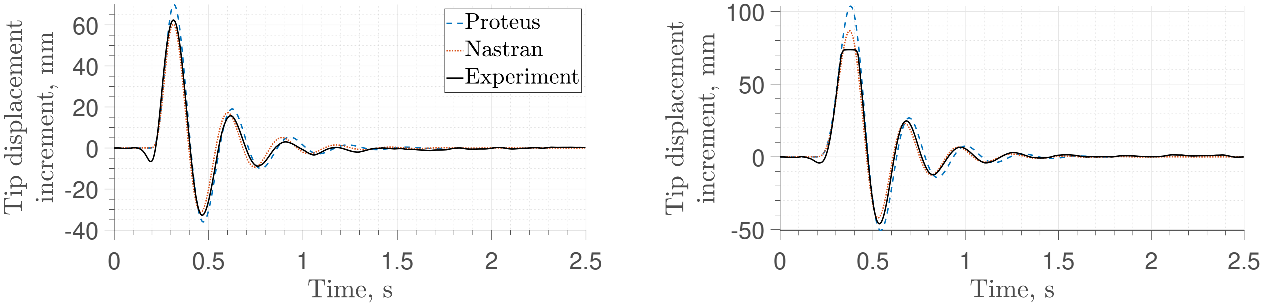

(a) Gust frequency: 8 Hz.

(b) Gust frequency: 4 Hz.

Fig. 16 Tip displacement history at 25 m/s with gust vanes angle of 10 deg.

VII. Conclusion

In this paper a methodology for the design of aeroelastically tailored composite wings employing a wingbox structure was presented and validated by means of a wind-tunnel experiment. The proposed methodology employs three different analysis tools: Proteus, a low-fidelity aeroelastic framework with tailoring capabilities, OptiBLESS, an open-source toolbox for optimization of blended stacking sequences and MSC Nastran, a commercial software commonly used in industry for aeroelastic analyses. A structural optimization involving aeroelastic tailoring is carried out with Proteus in the lamination parameters domain. The resulting optimized laminates are converted to a set of blended stacking sequences through OptiBLESS. Subsequently a medium-fidelity aeroelastic model is generated in Nastran, including the modelling of spar flanges and ribs, which is not accounted in Proteus. In this way, reliable buckling and crippling assessments are carried out in order to verify the safety of the design. The mentioned steps are repeated until all the safety criteria are met, each time adjusting the optimization constraints of Proteus in terms of strain and buckling applying correction factors derived using the medium-fidelity results. These factors are obtained comparing the strain levels and the buckling indices of the Proteus and Nastran model.

The proposed methodology was applied to the design of an experimental wing with a rectangular planform. The results of the final design loop were presented, with a focus on the changes in thickness and stiffness occurring due to the retrieval of blended stacking sequences. Results from the aeroelastic Nastran model were also presented, demonstrating that the final design successfully met the buckling and crippling requirements. The designed wing was manufactured and tested at the Open Jet Facility of Delft University of Technology. Static wind-tunnel tests revealed an average error of 11.6% and 3.3% on the lift and bending moment coefficients predicted by Proteus with respect to the experimental results. Respectively, the average error of Nastran's predictions amounted to 8.9% and 2.1%. Dynamic tests were performed using 1-cosine gusts with different gust amplitudes, gust frequencies and free-stream velocities. The experimental results in terms of maximum incremental lift coefficient, bending moment coefficient and tip displacement were compared with the numerical predictions. As far as Proteus is concerned, the numerical predictions showed average errors of 3.8%, -1.0% and 6.9% for the mentioned quantities, respectively. The corresponding errors associated with Nastran's predictions amounted to -9.4%, -5.2% and -13.7%.

Overall, the proposed methodology was successfully applied to the design of an aeroelastically tailored wing with a winbox structure. The static and dynamic wind-tunnel tests carried out provide experimental validation data for composite aeroelastically tailored wings and offer scope for improvement of the aeroelastic analysis and design framework developed at the Delft University of Technology.

Appendix: Optimization Parameters

In this appendix, the optimization parameters are given in detail.

The objective function is defined as a combination of weight minimization and wing tip displacement maximization:

$$\text{minimize} \quad f(\boldsymbol{x}) = -\frac{\Delta z_{tip}}{\Delta z_{tip,0}} w + \frac{W}{W_0}(1-w), \tag{9}$$

where Δz_{tip} is he tip displacement for load case #1, W is the wing weight and the subscript 0 indicates the values of the initial design. w is the optimization weight, which is set to 0.5 for the present study. The globally convergent method of moving asymptotes developed by Svanberg [34] is used as a gradient based optimiser.

Knockdown factors of 0.65 and 0.8 are applied to the material stress allowables to account for damage and environment. The knockdown factor related to material scatter is not applied because it is already taken into account by the method used to evaluate the fatigue constraint.

A summary of the initial values and bounds for thicknesses of top and bottom skin is given in Table 10. The lamination parameters are initially defined in such a way to provide quasi-isotropic stiffness distribution for all laminates.

Table 10 Initial values and bounds of laminates' thickness for Proteus optimization.

	Design region #		
	1	2	3
Initial value, mm	2.096	1.310	0.524
Min thickness, mm (# plies)	0.524 (4)	0.524 (4)	0.524 (4)
Max thickness, mm (# plies)	2.096 (16)	2.096 (16)	2.096 (16)

Lamination feasibility is included in the constraints to ensure realistic ply distributions. The equations used are the ones formulated by Hammer et al. [35], Raju et al. [36] and Wu et al. [37]. The static strength of the laminates is assessed by means of the Tsai-Wu criterion for the lamination parameter domain formulated by Khani et al. [38]. The idealized buckling model defined by Dillinger et al. [39] is employed to evaluate the buckling stability of the laminate panel.

For the last optimization of the design loop, the correction coefficients used for strain and buckling constraints are 0.75 and 0.35, respectively (calculated from the results of the previous iteration). The history of the last optimization is shown in Figure 17. The strain and buckling constraints are shown in terms of augmented strain and buckling indices, respectively $h_s \cdot 1.5 \cdot k_s$ and $h_b \cdot 1.5 \cdot k_b$, such that failure corresponds to an index of 1.

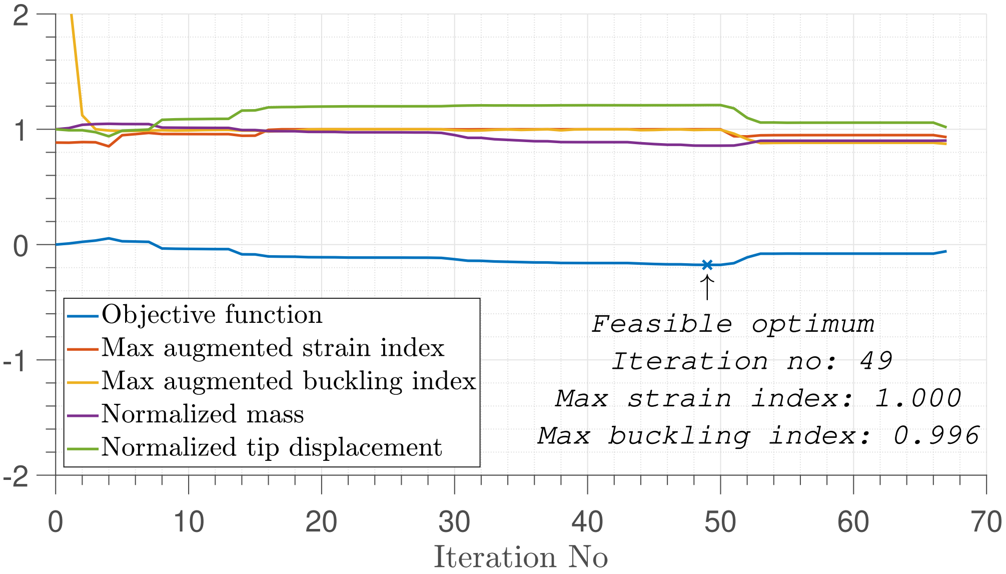

Fig. 17 History of last optimization of the design loop.

Acknowledgments

The authors would like to thank Paul Lancelot for the support with aeroelastic modelling in Nastran. The help of Christos Kassapoglou for the crippling assessment is also acknowledged by the authors. Finally, the authors would like to thank Nando Timmer for the support with the selection of the zig-zag tapes used in the wind-tunnel experiment.

References

[1] European Commission, "Flightpath 2050 Europe's Vision for Aviation," `https://www.acare4europe.org/sites/acare4europe.org/files/document/Flightpath2050_Final.pdf`, 2011.

[2] Del Rosario, R., Koudelka, J. M., Wahls, R., and Madavan, N., "NASA Fixed Wing Project: Green Technologies for Future Aircraft Generation," `https://ntrs.nasa.gov/archive/nasa/casi.ntrs.nasa.gov/20140012552.pdf`, Jan 2014. Oral Presentation SciTech2014.

[3] Jutte, C., and Stanford, B. K., "Aeroelastic Tailoring of Transport Aircraft Wings: State-of-the-Art and Potential Enabling Technologies," Tech. Rep. NASA/TM-2014-218252, NASA Langley Research Center, Apr 2014.

[4] Sherrer, V. C., Hertz, T. J., and Shirk, M. H., "Wind Tunnel Demonstration of Aeroelastic Tailoring Applied to Forward Swept Wings," *Journal of Aircraft*, Vol. 18, No. 11, 1981, pp. 976–983. doi:10.2514/3.57589, URL `https://doi.org/10.2514/3.57589`.

[5] Blair, M., and Weisshaar, T. A., "Swept composite wing aeroelastic divergence experiments," *Journal of Aircraft*, Vol. 19, No. 11, 1982, pp. 1019–1024. doi:10.2514/3.44806, URL `https://doi.org/10.2514/3.44806`.

[6] Hollowell, S. J., and Dugundji, J., "Aeroelastic flutter and divergence of stiffness coupled, graphite/epoxy cantilevered plates," *Journal of Aircraft*, Vol. 21, No. 1, 1984, pp. 69–76. doi:10.2514/3.48224, URL `https://doi.org/10.2514/3.48224`.

[7] Landsberger, B. J., and Dugundji, J., "Experimental aeroelastic behavior of unswept and forward-swept cantilever graphite/epoxy wings," *Journal of Aircraft*, Vol. 22, No. 8, 1985, pp. 679–686. doi:10.2514/3.45186, URL `https://doi.org/10.2514/3.45186`.

[8] Chen, G.-S., and Dugundji, J., "Experimental aeroelastic behavior of forward-swept graphite/epoxy wings with rigid-body freedom," *Journal of Aircraft*, Vol. 24, No. 7, 1987, pp. 454–462. doi:10.2514/3.45501, URL `https://doi.org/10.2514/3.45501`.

[9] Meddaikar, Y. M., Dillinger, J. K., Sodja, J., Mai, H., and Breuker, R. D., *Optimization, Manufacturing and Testing of a Composite Wing with Maximized Tip Deflection*, 2016. doi:10.2514/6.2016-0489, URL `https://arc.aiaa.org/doi/abs/10.2514/6.2016-0489`.

[10] Meddaikar, Y., Dillinger, J., Ritter, M., and Govers, Y., "Optimization & Testing of Aeroelastically-Tailored Forward Swept Wings," *International Forum on Aeroelasticity and Structural Dynamics IFASD 2017*, Como - Italy, 2017.

[11] Werter, N., and De Breuker, R., "A novel dynamic aeroelastic framework for aeroelastic tailoring and structural optimisation," *Composite Structures*, Vol. 158, 2016, pp. 369 – 386. doi:https://doi.org/10.1016/j.compstruct.2016.09.044, URL `http://www.sciencedirect.com/science/article/pii/S0263822316318669`.

[12] Werter, N. P. M., Sodja, J., and De Breuker, R., "Design and Testing of Aeroelastically Tailored Wings Under Maneuver Loading," *AIAA Journal*, Vol. 55, No. 3, 2017, pp. 1012–1025. doi:10.2514/1.J054965, URL `https://doi.org/10.2514/1.J054965`.

[13] Sodja, J., Werter, N., Dillinger, J. K., and Breuker, R. D., *Dynamic Response of Aeroelastically Tailored Composite Wing: Analysis and Experiment*, 2016. doi:10.2514/6.2016-0469, URL `https://arc.aiaa.org/doi/abs/10.2514/6.2016-0469`.

[14] Timmermans, H. S., van Tongeren, J. H., Geurts, E. G. M., Marques, R. F. A., Correa, M. S., and Waitz, S., "Design and Validation of a Numerical High Aspect Ratio Aeroelastic Wing Tunnel Model (HMAE1)," *International Forum on Aeroelasticity and Structural Dynamics IFASD 2019*, Savannah, Georgia, USA, 2019.

[15] Tang, D., and Dowell, E. H., "Experimental and Theoretical Study of Gust Response for High-Aspect-Ratio Wing," *AIAA Journal*, Vol. 40, No. 3, 2002, pp. 419–429. doi:10.2514/2.1691, URL `https://doi.org/10.2514/2.1691`.

[16] Tang, D., Grasch, A., and Dowell, E. H., "Gust Response for Flexibly Suspended High-Aspect Ratio Wings," *AIAA Journal*, Vol. 48, No. 10, 2010, pp. 2430–2444. doi:10.2514/1.J050309, URL `https://doi.org/10.2514/1.J050309`.

[17] Liu, Y., Xie, C., Yang, C., and Cheng, J., "Gust response analysis and wind tunnel test for a high-aspect ratio wing," *Chinese Journal of Aeronautics*, Vol. 29, No. 1, 2016, pp. 91 – 103. doi:https://doi.org/10.1016/j.cja.2015.12.013, URL `http://www.sciencedirect.com/science/article/pii/S1000936115002423`.

[18] Bi, Y., Xie, C., An, C., and Yang, C., "Gust load alleviation wind tunnel tests of a large-aspect-ratio flexible wing with piezoelectric control," *Chinese Journal of Aeronautics*, Vol. 30, No. 1, 2017, pp. 292 – 309. doi:https://doi.org/10.1016/j.cja.2016.12.028, URL `http://www.sciencedirect.com/science/article/pii/S1000936116302540`.

[19] Cheung, R. C. M., Rezgui, D., Cooper, J. E., and Wilson, T., "Testing of a Hinged Wingtip Device for Gust Loads Alleviation," *Journal of Aircraft*, Vol. 55, No. 5, 2018, pp. 2050–2067. doi:10.2514/1.C034811, URL `https://doi.org/10.2514/1.C034811`.

[20] Freydin, M., Rattner, M. K., Raveh, D. E., Kressel, I., Davidi, R., and Tur, M., "Fiber-Optics-Based Aeroelastic Shape Sensing," *AIAA Journal*, Vol. 0, No. 0, 2019, pp. 1–10. doi:10.2514/1.J057944, URL `https://doi.org/10.2514/1.J057944`.

[21] Ferede, E., and Abdalla, M., *Cross-sectional modelling of thin-walled composite beams*, 2014. doi:10.2514/6.2014-0163, URL `https://arc.aiaa.org/doi/abs/10.2514/6.2014-0163`.

[22] Macquart, T., "OPTIBLESS: An Open-source Toolbox for the Optimisation of Blended Stacking Sequence," *ECCM17 - 17th European Conference on Composite Materials*, European Conference on Composite Materials, ECCM, 2016.

[23] Macquart, T., Werter, N., and De Breuker, R., "Aeroelastic Design of Blended Composite Structures Using Lamination Parameters," *Journal of Aircraft*, Vol. 54, No. 2, 2017, pp. 561–571. doi:10.2514/1.C033859, URL `https://doi.org/10.2514/1.C033859`.

[24] Kassapoglou, C., *Design and Analysis of Composite Structures: With Applications to Aerospace Structures*, 2^{nd} ed., Aerospace Series, Wiley, John Wiley & Sons Ltd, The Atrium, Southern Gate, Chichester, West Sussex, PO19 8SQ, United Kingdom, 2013.

[25] Dillinger, J. K. S., "Static Aeroelastic Optimization of Composite Wings with Variable Stiffness Laminates," Ph.D. thesis, Delft University of Technology, 6 2014.

[26] Marlett, K., "Hexcel 8552 IM7 Unidirectional Prepreg 190 gsm & 35%RC Qualification Material Property Data Report," Data report, National Institute for Aviation Research, 2011.

[27] Rajpal, D., Gillebaart, E., and Breuker, R. D., "Preliminary aeroelastic design of composite wings subjected to critical gust loads," *Aerospace Science and Technology*, Vol. 85, 2019, pp. 96 – 112. doi:https://doi.org/10.1016/j.ast.2018.11.051, URL `http://www.sciencedirect.com/science/article/pii/S1270963818303948`.

[28] Rajpal, D., Kassapoglou, C., and Breuker, R. D., "Aeroelastic optimization of composite wings including fatigue loading requirements," *Composite Structures*, Vol. 227, 2019, p. 111248. doi:https://doi.org/10.1016/j.compstruct.2019.111248, URL `http://www.sciencedirect.com/science/article/pii/S0263822319317751`.

[29] Lignarolo, L. E. M., "On The Turbulent Mixing in Horizontal Axis Wind Turbine Wakes," Ph.D. thesis, Delft University of Technology, Apr 2016.

[30] Lancelot, P., Sodja, J., Werter, N., and De Breuker, R., "Design and testing of a low subsonic wind tunnel gust generator," *Advances in Aircraft and Spacecraft Science*, Vol. 4, No. 2, 2017, pp. 125–144. doi:10.12989/aas.2017.4.2.125, URL `http://dx.doi.org/10.12989/aas.2017.4.2.125`.

[31] Lancelot, P., Sodja, J., and De Breuker, R., "Investigation of the unsteady flow over a wing under gust excitation," *17th International Forum on Aeroelasticity and Structural Dynamics*, 2017. IFASD 2017 (Vol. 2017- June). [IFASD-2017-185] International Forum on Aeroelasticity and Structural Dynamics (IFASD).

[32] Braslow, A. L., and Know, E. C., "Simplified Method for Determination of Critical Height of Distributed Roughness Particles for Boundary-layer Transition at Mach Numbers from 0 to 5," Naca-tn-4363, National Advisory Committee for Aeronautics. Langley Aeronautical Lab.; Langley Field, VA, United States, 1958.

[33] Drela, M., "XFOIL: An Analysis and Design System for Low Reynolds Number Airfoils," *Low Reynolds Number Aerodynamics*, edited by T. J. Mueller, Springer Berlin Heidelberg, Berlin, Heidelberg, 1989, pp. 1–12.

[34] Svanberg, K., "A Class of Globally Convergent Optimization Methods Based on Conservative Convex Separable Approximations," *SIAM Journal on Optimization*, Vol. 12, No. 2, 2002, pp. 555–573. doi:10.1137/S1052623499362822, URL `https://doi.org/10.1137/S1052623499362822`.

[35] Hammer, V., Bendsøe, M., Lipton, R., and Pedersen, P., "Parametrization in laminate design for optimal compliance," *International Journal of Solids and Structures*, Vol. 34, No. 4, 1997, pp. 415 – 434. doi:https://doi.org/10.1016/S0020-7683(96)00023-6, URL `http://www.sciencedirect.com/science/article/pii/S0020768396000236`.

[36] Raju, G., Wu, Z., and Weaver, P., *On Further Developments of Feasible Region of Lamination Parameters for Symmetric Composite Laminates*, 2014. doi:10.2514/6.2014-1374, URL `https://arc.aiaa.org/doi/abs/10.2514/6.2014-1374`.

[37] Wu, Z., Raju, G., and Weaver, P. M., "Framework for the Buckling Optimization of Variable-Angle Tow Composite Plates," *AIAA Journal*, Vol. 53, No. 12, 2015, pp. 3788–3804. doi:10.2514/1.J054029, URL `https://doi.org/10.2514/1.J054029`.

[38] Khani, A., IJsselmuiden, S., Abdalla, M., and Gürdal, Z., "Design of variable stiffness panels for maximum strength using lamination parameters," *Composites Part B: Engineering*, Vol. 42, No. 3, 2011, pp. 546 – 552. doi:https://doi.org/10.1016/j.compositesb.2010.11.005, URL `http://www.sciencedirect.com/science/article/pii/S1359836810002131`.

[39] Dillinger, J. K. S., Klimmek, T., Abdalla, M. M., and Gürdal, Z., "Stiffness Optimization of Composite Wings with Aeroelastic Constraints," *Journal of Aircraft*, Vol. 50, No. 4, 2013, pp. 1159–1168. doi:10.2514/1.C032084, URL `https://doi.org/10.2514/1.C032084`.